

BRIGHT [C II] AND DUST EMISSION IN THREE $Z > 6.6$ QUASAR HOST GALAXIES OBSERVED BY ALMA

BRAM P. VENEMANS¹, FABIAN WALTER¹, LAURA ZSCHAECHNER¹, ROBERTO DECARLI¹, GISELLA DE ROSA^{2,3,4}, JOSEPH R. FINDLAY⁵, RICHARD G. MCMAHON^{6,7}, WILL J. SUTHERLAND⁸

Accepted for publication in ApJ

ABSTRACT

We present ALMA detections of the [C II] 158 μm emission line and the underlying far-infrared continuum of three quasars at $6.6 < z < 6.9$ selected from the VIKING survey. The [C II] line fluxes range between 1.6–3.4 Jy km s^{−1} ([C II] luminosities $\sim (1.9 - 3.9) \times 10^9 L_\odot$). We measure continuum flux densities of 0.56–3.29 mJy around 158 μm (rest-frame), with implied far-infrared luminosities between $(0.6 - 7.5) \times 10^{12} L_\odot$ and dust masses $M_d = (0.7 - 24) \times 10^8 M_\odot$. In one quasar we derive a dust temperature of 30^{+12}_{-9} K from the continuum slope, below the canonical value of 47 K. Assuming that the [C II] and continuum emission are powered by star formation, we find star-formation rates from 100–1600 $M_\odot \text{ yr}^{-1}$ based on local scaling relations. The $L_{[\text{CII}]} / L_{\text{FIR}}$ ratios in the quasar hosts span a wide range from $(0.3 - 4.6) \times 10^{-3}$, including one quasar with a ratio that is consistent with local star-forming galaxies. We find that the strength of the $L_{[\text{CII}]}$ and 158 μm continuum emission in $z \gtrsim 6$ quasar hosts correlate with the quasar’s bolometric luminosity. In one quasar, the [C II] line is significantly redshifted by $\sim 1700 \text{ km s}^{-1}$ with respect to the Mg II broad emission line. Comparing to values in the literature, we find that, on average, the Mg II is blueshifted by 480 km s^{-1} (with a standard deviation of 630 km s^{-1}) with respect to the host galaxy redshift, i.e. one of our quasars is an extreme outlier. Through modeling we can rule out a flat rotation curve for our brightest [C II] emitter. Finally, we find that the ratio of black hole mass to host galaxy (dynamical) mass is higher by a factor 3–4 (with significant scatter) than local relations.

Subject headings: cosmology: observations — galaxies: high-redshift — galaxies: ISM — galaxies: active — galaxies: individual (VIKING J234833.34–305410.0, J010953.13–304726.3, J030516.92–315056.0)

1. INTRODUCTION

One of the outstanding questions in astronomy is when the first galaxies formed, and what their physical properties were. In recent years, enormous progress has been made in finding galaxy candidates up to $z \gtrsim 10$, ~ 450 million years after the Big Bang (e.g., Robertson et al. 2010; Madau & Dickinson 2014). However, the extremely faint magnitudes (observed infrared magnitudes $J_{\text{AB}} \gtrsim 26$) and modest star formation rates (SFRs $\lesssim 10 M_\odot \text{ yr}^{-1}$) of these early galaxies make it nearly impossible to study the properties of the stars, gas and dust in much detail, even with current state-of-the-art facilities, including ALMA. An effective way to learn more about the constituents of galaxies at the highest redshifts is

to study the brightest (and most massive) members of this population ($L \gg L^*$). Such bright galaxies are very rare, and not found in the deep, pencil-beam searches typically used for high- z galaxy searches, e.g. with the *Hubble Space Telescope*.

In the local universe, it is argued that a tight correlation between the mass of a galaxy and the black hole that it harbors exist (e.g. see recent review by Kormendy & Ho 2013). Such a correlation seems to be in place also in the high redshift universe, at least to first order, as the host galaxies of bright quasars at $z > 2$ (powered by supermassive, $> 10^9 M_\odot$ black holes) are among the brightest and most massive galaxies found at these redshifts (e.g., Seymour et al. 2007; De Breuck et al. 2010; Mor et al. 2012). Therefore, an effective method to pinpoint the most massive and luminous galaxies in the early universe is believed to locate bright quasars at the highest redshifts. The Sloan Digital Sky Survey (SDSS) discovered ~ 30 bright ($M_{1450} < -26$) quasars around $z \sim 6$ which are shown to host supermassive, $> 10^9 M_\odot$ black holes (e.g., Fan et al. 2003, 2006; Jiang et al. 2007; Kurk et al. 2007; De Rosa et al. 2011). Observations of the host galaxies of these quasars in the radio and (sub)mm demonstrated that large reservoirs of dust and metal enriched atomic and molecular gas can exist in massive galaxies up to $z \sim 6.4$, less than 1 Gyr after the Big Bang (e.g., Bertoldi et al. 2003a,b; Walter et al. 2003; Maiolino et al. 2005; Wang et al. 2011, 2013). These observations already provide constraints on models of massive galaxy and dust for-

venemans@mpia.de

¹ Max-Planck Institute for Astronomy, Königstuhl 17, 69117 Heidelberg, Germany

² Department of Astronomy, The Ohio State University, 140 West 18th Avenue, Columbus, OH 43210, USA

³ Center for Cosmology and AstroParticle Physics, The Ohio State University, 191 West Woodruff Ave, Columbus, OH 43210, USA

⁴ Space Telescope Science Institute, 3700 San Martin Drive, Baltimore, MD 21218, USA

⁵ Department of Physics and Astronomy, University of Wyoming, Laramie, WY 82071, USA

⁶ Institute of Astronomy, University of Cambridge, Madingley Road, Cambridge CB3 0HA, UK

⁷ Kavli Institute for Cosmology, University of Cambridge, Madingley Road, Cambridge CB3 0HA, UK

⁸ School of Physics and Astronomy, Queen Mary University of London, Mile End Road, London, E1 4NS, UK

Table 1
Description of the ALMA observations

	J2348–3054	J0109–3047	J0305–3150
R.A. (J2000)	23 ^h 48 ^m 33 ^s 35	01 ^h 09 ^m 53 ^s 13	03 ^h 05 ^m 16 ^s 91
Decl. (J2000)	−30°54′10″28	−30°47′26″32	−31°50′55″94
$z_{\text{MgII}}^{\text{a}}$	6.889 ^{+0.007} _{−0.006}	6.747 ^{+0.007} _{−0.005}	6.605 ^{+0.002} _{−0.001}
ν_{obs} (GHz)	240.575	245.231	249.841
$t_{\text{exp, on-source}}$ (min)	17	16	16
# of antennas	18–30	23	23
RMS noise (per 100 MHz)	0.44 mJy	0.48 mJy	0.29 mJy
beam size	0′′74 × 0′′54	0′′70 × 0′′45	0′′62 × 0′′44

^a Taken from De Rosa et al. (2014)

mation at high redshift, requiring large initial gas masses and efficient supernova dust production (e.g., Maiolino et al. 2004; Michałowski et al. 2010; Gall et al. 2011; Kuo & Hirashita 2012; Valiante et al. 2014).

To further constrain the build-up of massive galaxies, the growth of supermassive black holes and the formation of dust in the early universe, it is important to locate and study bright quasars at the highest redshifts possible. Over the last four years, we have discovered seven quasars with redshifts above $z > 6.5$ (the SDSS limit) using wide-field near-infrared surveys with redshifts up to $z = 7.1$ (Mortlock et al. 2011; Venemans et al. 2013, 2015). These 7 quasars are currently the only known quasars at $z > 6.5$. These new $z > 6.5$ quasars are as bright as quasars at $z \sim 6$ and are powered by black holes with masses in excess of $\gtrsim 10^9 M_{\odot}$ (Mortlock et al. 2011; Venemans et al. 2013, 2015; De Rosa et al. 2014), constraining models of black hole formation (e.g., De Rosa et al. 2014).

In this paper, we report the detection of bright [C II] and dust continuum emission in three quasars at $z > 6.6$. These are VIKING J234833.34–305410.0 (hereafter J2348–3054), VIKING J010953.13–304726.3 (hereafter J0109–3040), and VIKING J030516.92–315056.0 (hereafter J0305–3150), discovered in Venemans et al. (2013). The paper is organized as follows. In Section 2 we describe the ALMA Cycle 1 observations. In Section 3 we present our results: in Section 3.1 we provide the detailed luminosities for each source, followed by a description of additional sources in the quasars fields in Section 3.5. In Section 4 we discuss our findings: firstly, in Section 4.1 we compare the [C II]/ L_{FIR} ratios of $z > 6.5$ quasar hosts with lower redshift counterparts, followed by a discussion of possible correlations between optical/near-infrared and far-infrared properties of high redshift quasars in Section 4.2. In Section 4.3 we look into the difference in redshift given by the rest-frame UV Mg II and far-infrared [C II] lines. In Section 4.4 we investigate the properties of the source detected with the highest significance, J0305–3150, followed by a discussion on the effects of the cosmic microwave background (CMB) on the observations in Section 4.5. In Section 4.6 we estimate dynamical masses of the quasar host galaxies using the detected [C II] lines. We conclude with a summary in Section 5.

Throughout this paper, we adopt the following cosmological parameters: $H_0 = 70 \text{ km s}^{-1} \text{ Mpc}^{-1}$, $\Omega_M = 0.28$, and $\Omega_{\Lambda} = 0.72$ (Komatsu et al. 2011). Star formation rates (SFRs) are calculated assuming a Kroupa & Weidner (2003) initial mass function (IMF).

2. ALMA OBSERVATIONS

Observations of the three $6.6 < z < 6.9$ quasars were carried out between 2013 July 5 and 2013 November 14. The setup of the observations for each of the sources was to have two overlapping sidebands covering the [C II] line (tuned using the Mg II redshift). The expected frequency of the [C II] line was 240.9, 245.3, and 250.1 GHz for J2348–3054, J0109–3047, and J0305–3150, respectively. The overlap between the two bandpasses was 20%, leaving a total frequency coverage of 3.375 GHz around the expected frequency of the [C II] line. At $z \sim 6.7$, this frequency coverage corresponds to $\sim 4100 \text{ km s}^{-1}$. The other two bandpasses were placed at approximately 15 GHz (observed) below the [C II] frequency to measure the far-infrared (FIR) continuum.

The observations were carried out in a compact configuration (baselines below 1 km and mostly below 300 m). The number of antennas used varied between 18 in July 2013 to 30 in November 2013. Bandpass calibration was performed through observations of J0334–4008, J0522–3627, and J2258–2758. For the flux and amplitude calibration, the sources J2357–5311, J0334–401, and Neptune were observed. The pointing was checked on sources J0120–2701, J0334–4008, J2357–5311, J0522–3627, and J2258–2758. Finally, the phase calibrators J0120–2701, J0334–4008, and J2339–3310 were observed every 7–8 min. The total on-source integration times on the quasars were 16–17 min per source.

Standard reduction steps using the Common Astronomy Software Applications package (CASA) were followed. Some flagging due to atmospheric lines was required, although such flagging was kept to a minimum in order to keep as much of the bandwidth as possible. Minimal additional flagging was required. High-frequency striping was present in the data, which was eliminated by removing the long baselines. Self-calibration was attempted with and without the long baselines, but showed no additional improvement and thus was not used for the final cubes. The cubes were cleaned using a weighting factor of robust=0.5, which optimized the noise per frequency bin and the resolution of the resulting map.

A summary of the observation is provided in Table 1.

3. RESULTS

3.1. [CII] and FIR emission

All three quasars are detected in the ALMA data in both the continuum and line emission. In Fig. 1 we show the spectrum of the brightest pixel in the spectral regions encompassing the [C II] line after smoothing the

Table 2
Far-infrared Properties of The $z > 6.6$ Quasars

	J2348–3054	J0109–3047	J0305–3150
[C II] redshift	6.9018 ± 0.0007	6.7909 ± 0.0004	6.6145 ± 0.0001
[C II]-Mg II velocity shift [km s ⁻¹]	486 ± 267	1690 ± 232	374 ± 79
[C II] line width (FWHM) [km s ⁻¹]	405 ± 69	340 ± 36	255 ± 12
[C II] line flux [Jy km s ⁻¹]	1.57 ± 0.26	2.04 ± 0.20	3.44 ± 0.15
Continuum flux density ^a [mJy]	1.92 ± 0.14	0.56 ± 0.11	3.29 ± 0.10
[C II] equivalent width (EW _[CII]) [μ m]	0.43 ± 0.08	1.90 ± 0.42	0.55 ± 0.03
[C II] luminosity [$10^9 L_\odot$]	1.9 ± 0.3	2.4 ± 0.2	3.9 ± 0.2
FIR luminosity [$10^{12} L_\odot$]	$2.4 - 4.9$	$0.6 - 1.5$	$4.0 - 7.5^b$
TIR luminosity [$10^{12} L_\odot$]	$3.8 - 6.9$	$0.9 - 2.2$	$6.3 - 10.6^b$
$L_{[CII]}/L_{FIR}$	$(0.33 - 0.94) \times 10^{-3}$	$(1.4 - 4.6) \times 10^{-3}$	$(0.50 - 1.03) \times 10^{-3b}$
SFR _{TIR} [M_\odot yr ⁻¹]	$555 - 1020$	$140 - 325$	$940 - 1580^b$
SFR _[CII] [M_\odot yr ⁻¹]	$100 - 680$	$140 - 895$	$250 - 1585$
M_{dust} [$10^8 M_\odot$]	$2.7 - 15$	$0.7 - 4.9$	$4.5 - 24$
Deconvolved size [C II]	$<0''.74 \times 0''.54^c$	$(0''.43 \pm 0''.10) \times (0''.39 \pm 0''.15)$	$(0''.60 \pm 0''.03) \times (0''.42 \pm 0''.04)$
Deconvolved size [C II] [kpc]	$<4.0 \times 2.9^c$	$(2.3 \pm 0.5) \times (2.1 \pm 0.8)$	$(3.3 \pm 0.2) \times (2.3 \pm 0.2)$
Deconvolved size continuum	$<0''.76 \times 0''.53^c$	$<0''.71 \times 0''.45^c$	$(0''.40 \pm 0''.02) \times (0''.29 \pm 0''.02)$
Deconvolved size continuum [kpc]	$<4.1 \times 2.9^c$	$<3.9 \times 2.5^c$	$(2.2 \pm 0.1) \times (1.6 \pm 0.1)$

^a Continuum flux density at a rest-frame wavelength of 158μ m.

^b In Section 4.5 we obtain $T_d = 30^{+12}_{-9}$ K by fitting the continuum slope of J0305–3150 while taking the effects of the cosmic microwave background into account. With a dust temperature of $T_d = 30$ K, we derive $L_{FIR} = 2.6 \times 10^{12} L_\odot$, $L_{TIR} = 3.7 \times 10^{12} L_\odot$, $L_{[CII]}/L_{FIR} = 1.5 \times 10^{-3}$, and $SFR_{TIR} = 545 M_\odot \text{ yr}^{-1}$.

^c Unresolved

data cubes with a $1''$ Gaussian using the CASA task ‘imsmooth’. We fitted a Gaussian + constant to the spectra to model the [C II] emission and the continuum. The Gaussian fit provided the redshift, width, and strength of the emission line, which are listed in Table 2. We averaged the continuum subtracted data cubes over the FWHM around the line centre to produce a map of the line emission (Fig. 2). The channels in bandpasses 0 and 1 that did not contain line emission, and bandpasses 2 and 3 were averaged to create maps of the continuum emission, which are also shown in Fig. 2. From the maps we measured the sizes of the line and continuum emission using CASA task ‘imfit’.

To derive far-infrared properties of the quasar hosts, we applied the same assumptions as Venemans et al. (2012). In short, the far-infrared luminosity (L_{FIR}) is defined as the luminosity integrated from 42.5μ m to 122.5μ m in the rest-frame (e.g., Helou et al. 1988). The total infrared luminosity (L_{TIR}) was computed by integrating the continuum from 8μ m to 1000μ m in the rest-frame. For the shape of the infrared continuum, we assumed three different models. The first is a modified black body: $f_\nu \propto B_\nu(T_d)(1 - e^{-\tau_d})$ with B_ν the Planck function with a dust temperature T_d and τ_d the dust optical depth (e.g., Beelen et al. 2006). Following the literature, our modified black body model has a dust temperature of $T_d = 47$ K and a dust emissivity power-law spectral index of $\beta = 1.6$ (see e.g., Beelen et al. 2006; Leipski et al. 2013). We further assume that the dust optical depth is low at far-infrared wavelengths, $\tau \ll 1$, at $\lambda > 40 \mu$ m. The other two models are templates of the local star-forming galaxies Arp 220 and M82 (Silva et al. 1998). Note that while the dust temperature of Arp 220 is found to be higher than the temperature assumed for our modified black body model, $T_d(\text{Arp220}) = 66$ K, the dust opacity is also higher with $\tau_d \approx 2$ at 158μ m (e.g., Rangwala et al. 2011). We show the three different templates, combined with the rest-frame UV and optical

photometry of the quasars, in Fig. 3. We caution that the range of values of L_{FIR} and L_{TIR} for the VIKING quasar hosts presented here strongly depends on our choice of models, see also Section 4.5. Additional far-infrared photometry is required to better constrain the shape of the infrared continuum and thus L_{FIR} and L_{TIR} .

If we assume that the continuum flux density measured around 158μ m arises from star formation (which seems to be a valid assumption for FIR detected quasars at $z > 5$, see e.g., Leipski et al. 2014; Barnett et al. 2015), then we can use the local scaling relation between SFR and L_{TIR} from Murphy et al. (2011) to obtain a measurement of the SFR in the quasar host: $SFR_{TIR}/M_\odot \text{ yr}^{-1} = 3.88 \times 10^{-44} L_{TIR}/\text{erg s}^{-1}$. Alternatively, we can use the [C II] emission to calculate the SFR by applying the relation between [C II] luminosity and SFR found by De Looze et al. (2014) for high redshift ($0.5 < z \lesssim 6$) galaxies: $SFR_{[CII]}/M_\odot \text{ yr}^{-1} = 3.0 \times 10^{-9} (L_{[CII]}/L_\odot)^{1.18}$, with an uncertainty of 0.4 dex. Using instead the relation between SFR and $L_{[CII]}$ derived by de Looze et al. (2011) and Sargsyan et al. (2014) the SFRs would be a factor ~ 2 – 2.5 lower. The reason for this difference is that the latter relations are derived for star-forming galaxies with SFRs below $\lesssim 100 M_\odot \text{ yr}^{-1}$ and FIR luminosities $L_{FIR} \lesssim 10^{12} L_\odot$ and might not be applicable for our high redshift, $L_{FIR} \gtrsim 10^{12} L_\odot$ quasar hosts (see, e.g., the discussion in De Looze et al. 2014). Similarly, if we apply the relation derived by Herrera-Camus et al. (2015) for 46 local galaxies with $L_{TIR} < 10^{11} L_\odot$, then the resulting SFR_[CII] are a factor ~ 5 – 6 lower. They suggest that sources with $10^{11} < L_{TIR} < 10^{12} L_\odot$ have a relation that is a factor 1.9 higher, which would give roughly similar SFRs as de Looze et al. (2011) and Sargsyan et al. (2014). Finally, we derived total dust masses both by using the M82 and Arp220 templates and by assuming a dust temperature of 47 K and a dust mass opacity coefficient of $\kappa_\lambda = 0.77 (850 \mu\text{m}/\lambda)^\beta \text{ cm}^2 \text{ g}^{-1}$ (Dunne et al. 2000). Since the dust temperatures in these quasar host

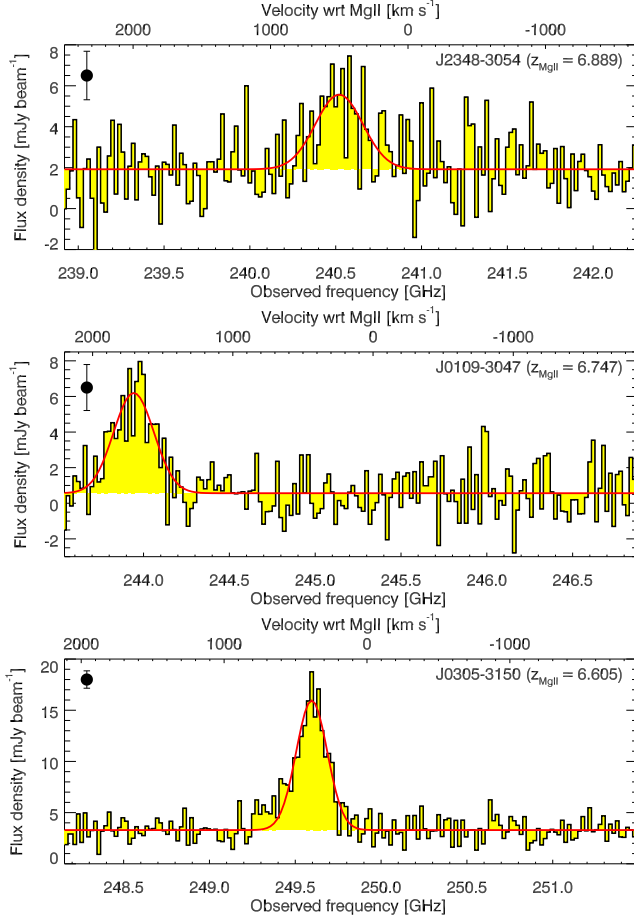


Figure 1. [C II] spectra of the three $z > 6.6$ quasars observed with ALMA. The spectra were extracted from the data cubes smoothed with a $1''$ Gaussian at the location of the brightest pixel in the emission line map (Fig. 2), which in all cases coincides with the optical/near-infrared position of the quasars. Only the two band-passes encompassing the emission line are shown. The bottom axis shows the observed frequency in GHz and on the top we plot the velocity with respect to the redshift of the Mg II line, which is also given in the top right corner of each spectrum. The solid line represents a Gaussian+continuum fit to the data. The typical uncertainty per bin is plotted in the upper left corner of each spectrum.

is assumed to be significantly higher than the temperature of the CMB at these redshifts, $T_{\text{CMB}}(z = 6.7) \approx 21$ K, we ignore the effect of the CMB on the ALMA observations in Sections 3.2–3.4 (but see da Cunha et al. 2013). We will however further address the effects of the CMB in Section 4.4.3. The results are also summarized in Table 2.

3.2. J2348–3054

J2348–3054 is the highest redshift quasar of our sample, with $z_{\text{MgII}} = 6.889$ (Venemans et al. 2013; De Rosa et al. 2014). The [C II] emission line is detected with a peak signal-to-noise $S/N \sim 10$ at $z_{\text{[CII]}} = 6.9018 \pm 0.0007$ (Fig. 2). The emission line has a peak flux density of $f_p = 3.64 \pm 0.52$ mJy beam $^{-1}$ and a FWHM of 405 ± 69 km s $^{-1}$. The line emission is unresolved within the $0''.74 \times 0''.54$ beam (see also Fig. 4). The integrated line flux derived from the Gaussian fit to the spectrum (Fig. 1) is $F_{\text{[CII]}} = 1.57 \pm 0.26$ Jy km s $^{-1}$ which corresponds to a luminosity of $L_{\text{[CII]}} = (1.9 \pm 0.3) \times 10^9 L_{\odot}$, ap-

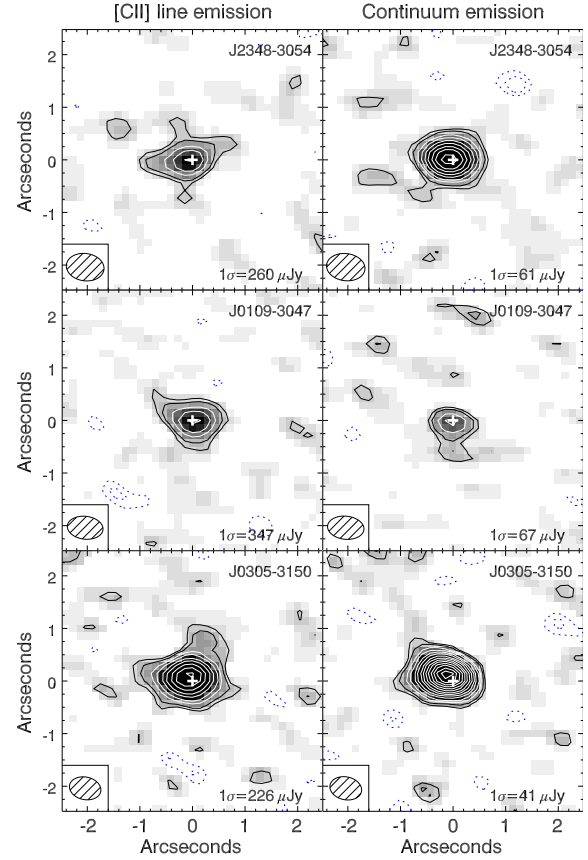


Figure 2. Maps of the line emission (left) and continuum (right) of the VIKING quasars. For the line maps the line emission was averaged over the FWHM, measured from the spectrum of the central pixel (Fig. 1 and Table 2), and the continuum emission was subtracted. The beam is shown in the bottom left of each map. The emission was averaged over 450 km s $^{-1}$, 330 km s $^{-1}$, and 225 km s $^{-1}$ in the case of J2348–3054, J0109–3047, and J0305–3150, respectively. The 1σ rms noise of each map is printed at the bottom right. The small white cross indicates the optical/near-infrared position of the quasar. The blue, dashed contours are -3σ and -2σ . The black, solid contours are $+2\sigma$ and $+3\sigma$, the white solid contours are $[5, 7, 10, 13, 17, 21, 26, 31, 37, 43, 50, 57] \times \sigma$.

proximately two times brighter than the $z = 7.1$ quasar J1120+0641 (Venemans et al. 2012).

The far-infrared continuum, measured from the line free channels in the spectrum, is detected with a flux density of $f_c = 1.92 \pm 0.14$ mJy. The continuum is also not resolved. The rest-frame [C II] equivalent width (EW) is $0.43 \pm 0.08 \mu\text{m}$, which is a factor ~ 2 below the median [C II] EW of starburst galaxies (which have median $\text{EW}_{\text{[CII]}} = 1.0 \mu\text{m}$, Sargsyan et al. 2014). The luminosity of the far-infrared emission depends on the assumed model for the dust emission. The modified black body ($T_d = 47$ K and $\beta = 1.6$) gives $L_{\text{FIR}} = (4.5 \pm 0.3) \times 10^{12} L_{\odot}$, while scaling the Arp220 and M82 templates to the observed continuum flux density results in a far-infrared luminosity of $(2.5 \pm 0.2) \times 10^{12} L_{\odot}$ and $(2.9 \pm 0.2) \times 10^{12} L_{\odot}$ respectively. We therefore estimate that L_{FIR} is in the range

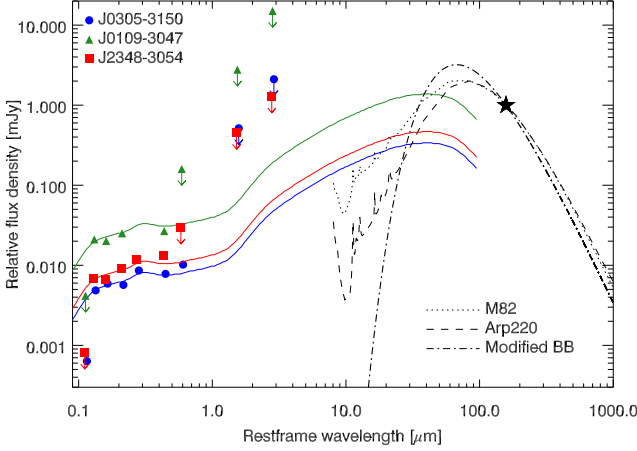


Figure 3. Spectral energy distributions (SEDs) of the three VIKING quasars, normalized to 1 mJy at 158 μm in the rest-frame. The rest-frame UV to near-infrared data points are taken from Venemans et al. (2013) and from the *Wide-field Infrared Survey Explorer* (WISE, Wright et al. 2010). We fitted the quasar template of Richards et al. (2006) to the short wavelength ($\lambda_{\text{obs}} < 30 \mu\text{m}$) data points of each quasar. The three models used in this paper to model the far-infrared emission are shown by the dotted (M82 template), dashed (Arp 220 template), and dot-dashed (modified black body) lines.

$(2.4 - 4.9) \times 10^{12} L_{\odot}$. The total infrared luminosity is calculated to be $(4.0 \pm 0.3) \times 10^{12} L_{\odot}$, $(6.3 \pm 0.5) \times 10^{12} L_{\odot}$, and $(6.4 \pm 0.5) \times 10^{12} L_{\odot}$ for the Arp220 template, the M82 template, and the modified black body, giving a range of $L_{\text{TIR}} = (3.8 - 6.9) \times 10^{12} L_{\odot}$. Assuming the total far-infrared emission is powered by star formation, this results in a $\text{SFR} = 555 - 1020 M_{\odot} \text{yr}^{-1}$. Applying the relation between $L_{[\text{CII}]}$ and SFR gives a lower SFR of $\text{SFR} = 270_{-170}^{+410} M_{\odot} \text{yr}^{-1}$. Combined with the SFR derived from the TIR luminosity, our best estimation of the SFR in this quasar host is $100 - 1020 M_{\odot} \text{yr}^{-1}$. The dust mass is estimated to be in the range $(2.7 - 15.5) \times 10^8 M_{\odot}$.

3.3. J0109-3047

The quasar J0109-3047 has the faintest absolute UV magnitude ($M_{\text{UV}} = -25.5$, Venemans et al. 2013) of our sample. From the Mg II line a redshift of $z = 6.747$ was derived (De Rosa et al. 2014). In the ALMA data the [C II] emission line is clearly detected with a peak S/N ≈ 11 (Fig. 2), but at a redshift of $z_{[\text{CII}]} = 6.7909 \pm 0.0004$, which is $1690 \pm 232 \text{ km s}^{-1}$ redward of the expected redshift based on the Mg II line. This is a significant offset, and we will discuss the shifts between the Mg II and [C II] lines in Section 4.3.

The [C II] line in the spectrum extracted from the brightest pixel in our smoothed data cube (Fig. 1) has a peak flux of $f_p = 5.6 \pm 0.5 \text{ mJy beam}^{-1}$ and a FWHM of $340 \pm 36 \text{ km s}^{-1}$. The line emission is marginally resolved (Fig. 4) in the $0''.70 \times 0''.45$ beam with a deconvolved size of $0.43 \pm 0.10 \text{ arcsec} \times 0.39 \pm 0.15 \text{ arcsec}$. At a redshift of $z = 6.79$ this corresponds to a size of $(2.3 \pm 0.5) \times (2.1 \pm 0.8) \text{ kpc}^2$. The integrated line flux is $F_{[\text{CII}]} = 2.04 \pm 0.20 \text{ Jy km s}^{-1}$, and the luminosity is $L_{[\text{CII}]} = (2.4 \pm 0.2) \times 10^9 L_{\odot}$, similar to the [C II] luminosity of J2348-3054.

The continuum is significantly fainter than that of the other two quasars, with a measured flux density of

$f_c = 0.56 \pm 0.11 \text{ mJy}$. The source is not resolved in the continuum map (Fig. 2). Given the moderate S/N = 7.2 of the continuum emission we cannot exclude that the size of the line and continuum emission are similar. The equivalent width of the [C II] line is $\text{EW} = 1.90 \pm 0.42 \mu\text{m}$, which is higher than the [C II] EW found for local starburst galaxies (Sargsyan et al. 2014).

Based on the three different models for the shape of the far-infrared emission and taking into account the uncertainty in the measured flux density, our best estimate of the far-infrared luminosity is $L_{\text{FIR}} = (0.6 - 1.5) \times 10^{12} L_{\odot}$, the total infrared luminosity is in the range $L_{\text{TIR}} = (0.9 - 2.2) \times 10^{12} L_{\odot}$, and the total mass of dust is $M_d = (0.7 - 4.9) \times 10^8 M_{\odot}$. From the infrared luminosity we derive a star formation rate of $\text{SFR} = 140 - 325 M_{\odot} \text{yr}^{-1}$. The strength of the [C II] line results in a similar SFR of $\text{SFR}_{[\text{CII}]} = 355_{-215}^{+540} M_{\odot} \text{yr}^{-1}$.

3.4. J0305-3150

J0305-3150 with $z_{\text{MgII}} = 6.605$ is the brightest of the three quasars with an absolute UV magnitude of $M_{\text{UV}} = -26.0$ (Venemans et al. 2013). In the ALMA data both the [C II] emission line and the far-infrared continuum are detected at high significance (S/N > 25, see Fig. 2). The [C II] line gives a redshift of the quasar host of $z_{[\text{CII}]} = 6.6145 \pm 0.0001$ (Fig. 1), which is slightly higher ($374 \pm 79 \text{ km s}^{-1}$) than that of the Mg II line.

The peak flux density of the [C II] line in Fig. 1 is $f_p = 12.7 \pm 0.5 \text{ mJy beam}^{-1}$. The line width is $\text{FWHM} = 255 \pm 12 \text{ km s}^{-1}$. The line emission is resolved with a deconvolved size of $(0.60 \pm 0.03) \times (0.42 \pm 0.04) \text{ arcsec}^2$, which corresponds to $(3.3 \pm 0.2) \times (2.3 \pm 0.2) \text{ kpc}^2$. The integrated line flux of $F_{[\text{CII}]} = 3.44 \pm 0.15 \text{ Jy km s}^{-1}$ is the highest of the three quasars and the [C II] luminosity of $L_{[\text{CII}]} = (3.9 \pm 0.2) \times 10^9 L_{\odot}$ is similar to that of the $z = 6.42$ quasar J1148+5251 ($L_{[\text{CII}]} = (4.1 \pm 0.3) \times 10^9 L_{\odot}$; Maiolino et al. 2005; Walter et al. 2009), making it one of the brightest [C II] emitters at $z > 6$. If the [C II] emission traces star formation activity, then the SFR is $\text{SFR}_{[\text{CII}]} = 630_{-380}^{+955} M_{\odot} \text{yr}^{-1}$. Taking the diameter of the line emitting region as $1.5 \times$ the deconvolved size (e.g., Wang et al. 2013), then we derive a source area of $\pi (0.75 a_{\text{maj}}) \times (0.75 a_{\text{min}}) = 14 \pm 2 \text{ kpc}^2$ with a_{maj} and a_{min} the deconvolved major and minor axis FWHM of the line emitting region (see Table 2). We determine a [C II] surface density of $\Sigma_{[\text{CII}]} = (2.9 \pm 0.4) \times 10^8 L_{\odot} \text{ kpc}^{-2}$ or $\Sigma_{[\text{CII}]} = (1.1 \pm 0.1) \times 10^{42} \text{ erg s}^{-1} \text{ kpc}^{-2}$. Applying the relation between [C II] surface density and star formation rate surface density from Herrera-Camus et al. (2015) and taking into account that galaxies with $L_{\text{TIR}} > 10^{11} L_{\odot}$ have a normalization that is a factor ~ 2 higher, we derive a SFR surface $\Sigma_{\text{SFR}} \sim 25 M_{\odot} \text{yr}^{-1} \text{ kpc}^{-2}$ and a total $\text{SFR}_{[\text{CII}]} \sim 335 M_{\odot} \text{yr}^{-1}$, approximately a factor two lower than our other [C II] SFR estimates.

In the map of the continuum emission (Fig. 2) we detect the quasar with a S/N = 62. The detection is at such high significance that we can even constrain the slope of the continuum emission of this source (see the discussion in Section 4.4.3). The continuum emission is also resolved and the deconvolved size of the source is $(0.40 \pm 0.02) \times (0.29 \pm 0.02) \text{ arcsec}^2$,

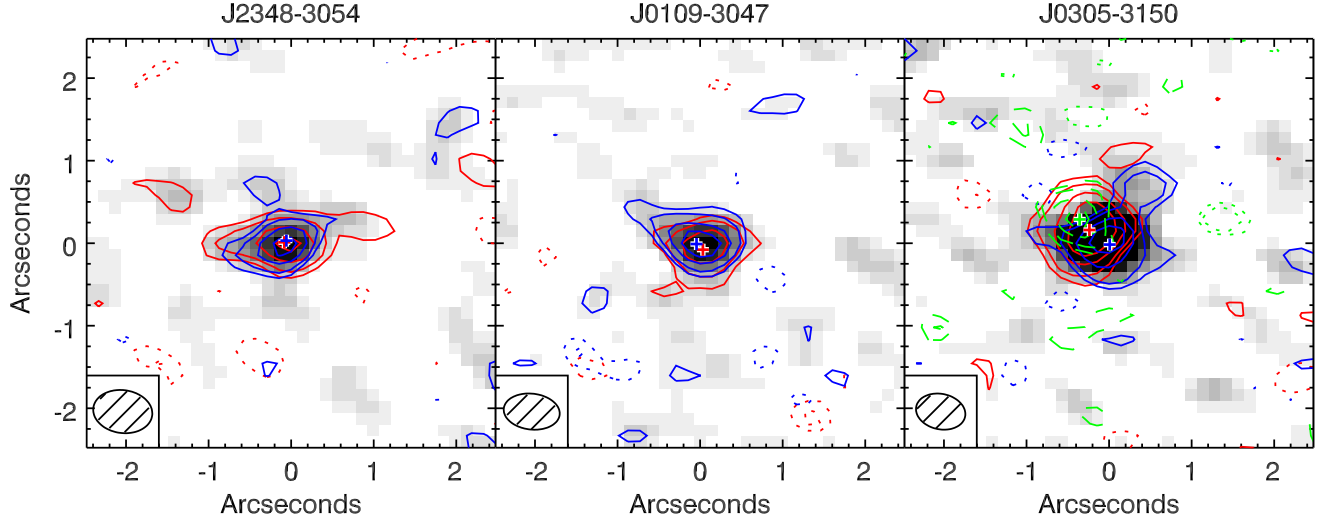


Figure 4. Contour plots of the line emission averaged of the FWHM (in grey scale) and the blue side and red side of the emission line (in blue and red contours). Contour levels are $[-3, -2, +2, +3, +5, +7, +10] \times \sigma$. In the case of J2348–3054 and J0109–3047 the blue side of the line was centered +81.3 MHz and +69.2 MHz ($+FWHM/4$) from the frequency of the line center and averaged over 162.6 MHz and 138.5 MHz ($FWHM/2$), respectively. The red side was centered –81.3 MHz and –69.2 MHz from the line center. For J0305–3150, the maps of the blue and red side of the line were constructed by averaging over 141.7 MHz ($2/3 \times FWHM$) centered +141.7 MHz and –141.7 MHz, respectively. For J0305–3150 we also show a map in green, long-dashed contours of the emission averaged from 249.25 GHz to 249.39 GHz. At these frequencies there appears to be an excess of emission over the Gaussian fit (see Fig. 1). We will discuss this emission in Section 4.4.2. No offsets between the red and blue emission are found for the quasars J2348–3054 and J0109–3047, but J0305–3150 shows indications for intrinsic gas motions on the scales resolved here (see also Section 4.4.1).

Table 3
Additional Continuum Sources in the Quasar Fields.

Field	R.A. (J2000)	Decl. (J2000)	Flux density	S/N	J_{AB}	$K_{s,AB}$
J2348–3054	23 ^h 48 ^m 32 ^s .92	–30°54′06″.52	0.65±0.06	10.6	>22.3 ^a	>21.5 ^a
J0305–3150	03 ^h 05 ^m 16 ^s .37	–31°50′54″.95	0.21±0.04	5.1	>22.1 ^a	>21.6 ^a
J0305–3150	03 ^h 05 ^m 17 ^s .11	–31°50′52″.10	0.20±0.04	4.9	>22.1 ^a	>21.6 ^a

^a 3σ magnitude limits

or $(2.2 \pm 0.1) \times (1.6 \pm 0.1) \text{ kpc}^2$. The object appears thus more extended in the line emission. This could indicate the presence of an additional component in the [C II] emission or dust heating by the central active galactic nucleus (AGN). We will discuss this further in Sections 4.1 and 4.2.

The continuum flux density measured in the spectrum (Fig. 1) is $f_c = 3.29 \pm 0.10 \text{ mJy}$, making this one of the brightest $z > 5.5$ quasars observed around 250 GHz (e.g., Wang et al. 2008). The [C II] equivalent width is $EW_{[CII]} = 0.55 \pm 0.03 \mu\text{m}$, a factor ~ 2 lower than that of local starbursts and similar to the $EW_{[CII]}$ measured in J2348–3054 (Section 3.2). From the measured continuum flux density we derive $L_{FIR} = (4.0 - 7.5) \times 10^{12} L_\odot$ and $L_{TIR} = (6.3 - 10.6) \times 10^{12} L_\odot$ (but see the discussion in Section 4.5). The total infrared luminosity results in an upper limit on the SFR of $SFR = 940 - 1580 M_\odot \text{ yr}^{-1}$. However, as will be discussed in Sections 4.4.3 and 4.5, the TIR luminosity in this quasar host might be overestimated. From the continuum slope we measured a dust temperature of 30 K, resulting in a lower L_{TIR} and implying a $SFR_{TIR} = 545 M_\odot \text{ yr}^{-1}$, similar to the [C II] derived SFR. Finally, we estimate that the dust mass in this quasar host is in the range $M_d = (4.5 - 24) \times 10^8 M_\odot$.

3.5. Other sources in the field

We searched for other sources in the field of the quasars. We searched the data cubes for emission line sources and the continuum images for continuum sources.

3.5.1. Continuum Sources in the Field

The continuum images have rms values of $61 \mu\text{Jy beam}^{-1}$, $67 \mu\text{Jy beam}^{-1}$, and $42 \mu\text{Jy beam}^{-1}$ for J2348–3054, J0109–3047, and J0305–3150, respectively. The largest, negative noise peaks in the images have a $S/N = -4.3$. In the following we assume that sources with a $S/N > 4.5$ are real, and not due to noise fluctuations. In the three quasar fields we discovered three objects with a peak flux density above a $S/N > 4.5$. The coordinates and flux densities are listed in Table 3. We verified that these objects are not artifacts from the central quasar left over after cleaning. We have checked the NASA/IPAC Extragalactic Database (NED)⁹ and none of the sources had a counterparts in the database. Also, no associated near-infrared sources were found in the VIKING images down to $J_{AB} > 22.1$ and $K_{s,AB} > 21.5$ (see e.g., Venemans et al. 2013 for details about the VIKING survey).

⁹ <http://ned.ipac.caltech.edu>

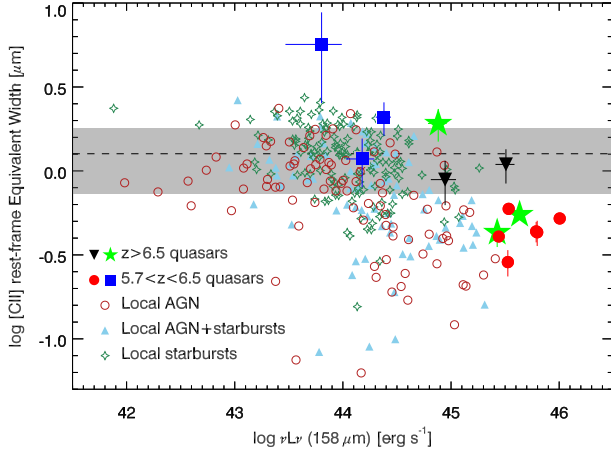


Figure 6. Rest-frame equivalent width (EW) of the [C II] line vs. monochromatic luminosity at a wavelength of $158\,\mu\text{m}$ (rest-frame). We plotted values for local systems (starburst galaxies as open stars, AGN as open circles and composite galaxies as filled triangles) from Díaz-Santos et al. (2013) and Sargsyan et al. (2014). We marked the mean and 1 sigma range found for local starburst galaxies with a dashed line and gray region. As in Fig. 5, the blue squares and red circles indicate the values found for quasars at $5.7 < z < 6.5$, while the green filled stars and black, upside down triangles are the VIKING quasars and two other $z > 6.5$ quasars. The high redshift quasars have [C II] EWs within a factor of ~ 5 of the mean of that of local starbursts.

to the quasars studied by Wang et al. (2013), J0109–3047 has a ratio consistent with star-forming galaxies. The range of characteristics of $z > 6.5$ quasar hosts is quite similar to that of $z > 2$ (ultra-)luminous infrared galaxies, roughly following the correlation between L_{FIR} and $L_{[\text{CII}]} / L_{\text{FIR}}$ discussed in Willott et al. (2015). A possible explanation for the decreasing $L_{[\text{CII}]} / L_{\text{FIR}}$ ratio as function of increasing L_{FIR} could be that in the $z \gtrsim 6$ quasar hosts studied here and by, e.g., Wang et al. (2013) and Willott et al. (2015), at least a fraction of the FIR luminosity is due dust heating by the central AGN. Alternatively, the strong X-ray radiation from the central source could affect the C^+ abundance, reducing the [C II] luminosity (e.g., Langer & Pineda 2015).

An issue with the [C II]–to–FIR luminosity ratio in the $z > 5.7$ quasar hosts is the unknown shape of the far-infrared dust continuum, resulting in a highly uncertain estimate of the FIR luminosity (see Section 3.1). By analyzing the spectral energy distribution of far-infrared bright ($f_{\text{obs}}(1.2\text{mm}) > 1\text{ mJy}$) quasars at $z > 5$, Leipski et al. (2013) found dust temperature in the range $T_d = 40 - 60\text{ K}$. In the literature, a dust temperature of 47 K is regularly assumed, even for $z \sim 6$ quasar hosts with relative weak ($f_{\text{obs}}(1.2\text{mm}) \lesssim 0.2\text{ mJy}$) far-infrared continua (e.g., Willott et al. 2015). If the dust temperature varies significantly among different quasar host galaxies (see Section 4.4.3 for an example), the spread in $L_{[\text{CII}]} / L_{\text{FIR}}$ ratio could be larger than shown in Fig. 5.

A more direct measurement of the relative strength of the [C II] line with respect to the underlying continuum can be obtained from our data by dividing the line flux by the continuum flux density: the [C II] equivalent width (EW). The advantage of calculating the [C II] equivalent width over the $L_{[\text{CII}]} / L_{\text{FIR}}$ ratio is that it does not depend on the characteristics of the dust continuum emission. For our quasar hosts, we obtained rest-

frame [C II] equivalent widths between 0.43 and $1.9\,\mu\text{m}$ (Fig. 2). These values are within a factor of ~ 3 of the mean $\text{EW}_{[\text{CII}]} = 1.27\,\mu\text{m}$ found for local starburst galaxies (Fig. 6; Díaz-Santos et al. 2013; Sargsyan et al. 2014).

In the next section, we will compare the properties of the far-infrared emission of the quasar hosts with those of their nuclear source.

4.2. Correlations Between UV and FIR Properties

In Fig. 7 we compare the FIR properties ($L_{[\text{CII}]}$, L_{FIR} , and $L_{[\text{CII}]} / L_{\text{FIR}}$) of the $z > 5.7$ quasar hosts with the redshift and the characteristics of the accreting black hole (black hole mass M_{BH} and bolometric luminosity L_{bol} of the central AGN). The bolometric luminosity L_{bol} of the central AGN was computed by applying a bolometric correction to the monochromatic luminosity at 1450 Å in the rest-frame. The monochromatic luminosities were derived from published absolute magnitudes (Calura et al. 2014; Venemans et al. 2013, 2015), which have an assumed uncertainty of 15%. We derived the bolometric correction by taking the data from Table 1 in (Runnoe et al. 2012) and fitting a line of the form:

$$\log \left(\frac{L_{\text{bol}}}{10^{46} \text{ erg s}^{-1}} \right) = a + b \log \left(\frac{\lambda L_{\lambda}}{10^{46} \text{ erg s}^{-1}} \right). \quad (1)$$

We obtain $a = 0.459 \pm 0.017$ and $b = 0.911 \pm 0.022^{11}$ and use these parameters to compute L_{bol} from the monochromatic luminosity at $\lambda_{\text{rest}} = 1450\text{ Å}$.

The black hole masses of the VIKING quasars, estimated from the width of the Mg II line and the strength of the quasar’s continuum, were derived in De Rosa et al. (2014). For the other $z \sim 6$ quasars, black hole masses derived from the Mg II line were taken from the literature when available (Willott et al. 2010; De Rosa et al. 2011, 2014; Venemans et al. 2015). For objects for which no Mg II derived black hole masses are published, we assumed that the quasars are accreting at the Eddington luminosity ($L_{\text{Edd}} = 1.3 \times 10^{38} (M_{\text{BH}} / M_{\odot}) \text{ erg s}^{-1}$) as has been found for $z \sim 6$ quasars (e.g., Willott et al. 2010; De Rosa et al. 2011). To account for the range in Eddington ratios observed in these quasars, we added an uncertainty of 0.3 dex in quadrature to the uncertainty in the bolometric luminosity. For easy comparison we computed L_{FIR} assuming a modified black body with $T_d = 47\text{ K}$ and $\beta = 1.6$ for all sources (however, see Section 4.4.3 for a discussion on this assumption).

From the parameters plotted against each other in Fig. 7, four correlate strongly (defined by us as having a Pearson’s r of $|r| > 0.5$): M_{BH} with L_{FIR} or, more accurately, with the measured monochromatic luminosity at a rest-frame wavelength of $158\,\mu\text{m}$, $\nu L_{\nu, 158\,\mu\text{m}}$, M_{BH} with $L_{[\text{CII}]}$, and L_{bol} with L_{FIR} (or $\nu L_{\nu, 158\,\mu\text{m}}$) and $L_{[\text{CII}]}$. Since all quasars plotted in the figure are either accreting close to the Eddington limit or explicitly assumed to accrete at Eddington, the correlation between M_{BH} and L_{FIR} ($L_{[\text{CII}]}$) could be due to the correlations between

¹¹ In Runnoe et al. (2012) they fit a line $\log(L_{\text{iso}}) = a + b \log(\lambda L_{\lambda})$ with $L_{\text{iso}} = L_{\text{bol}} / 0.75$. In this form, a is determined where $\log(\lambda L_{\lambda}) = 0$, which is far from the range of λL_{λ} that was fitted. As a consequence, the uncertainty in a is large (1 dex) and the resulting uncertainty in L_{bol} computed using their best fit parameters is overestimated.

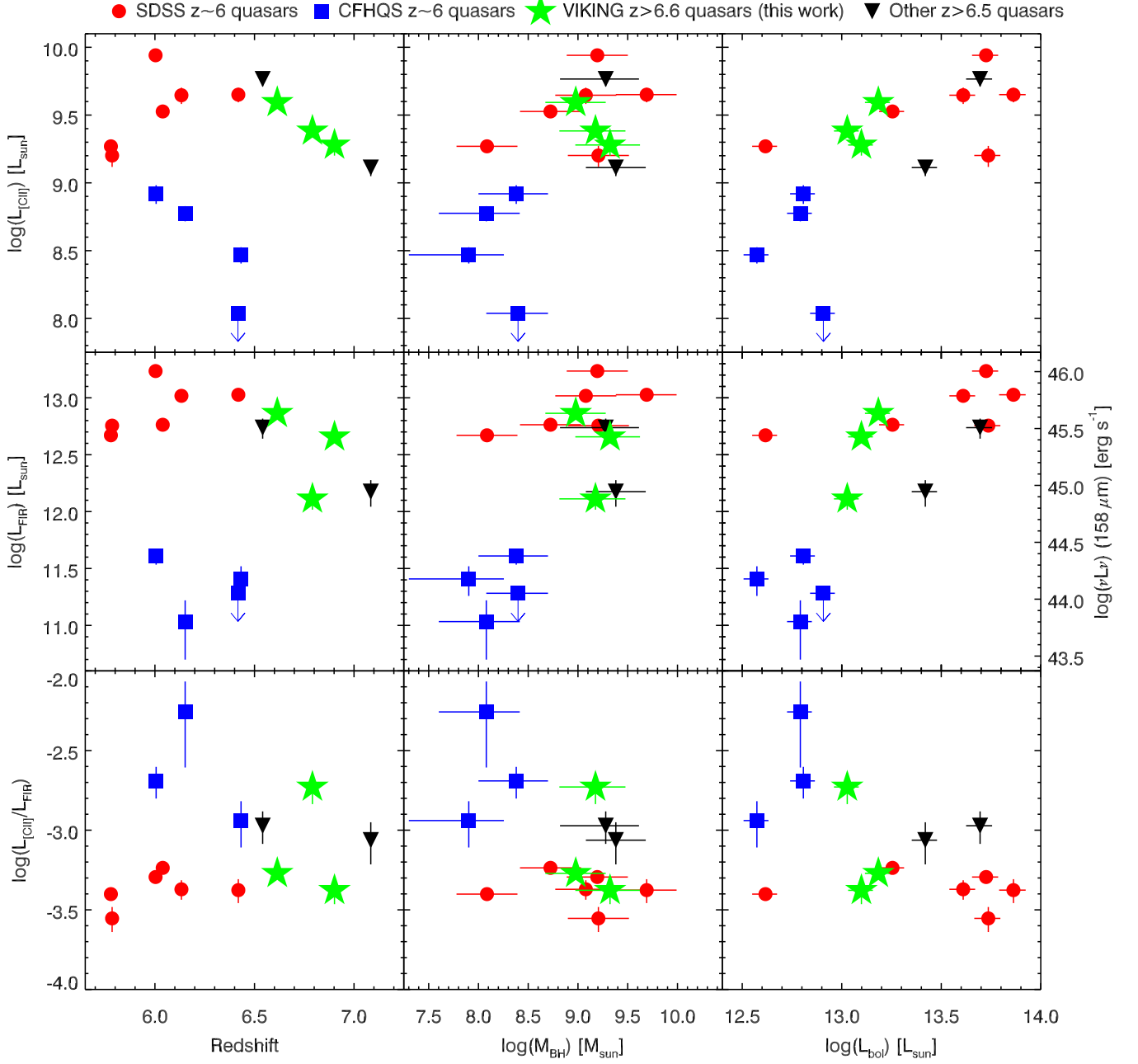


Figure 7. Host galaxy properties measured in the far-infrared (L_{CII} , L_{FIR} , and $L_{\text{CII}}/L_{\text{FIR}}$) plotted against the characteristics of the quasar (M_{BH} and L_{bol}) and redshift. The bolometric luminosity of the quasars was calculated by applying the bolometric correction to the absolute magnitudes at 1450 \AA in the rest-frame (M_{1450}) from Runnoe et al. (2012), with the absolute magnitudes taken from the literature (Calura et al. 2014; Venemans et al. 2013, 2015). The red circles represent the properties of $z \sim 6$ SDSS quasars observed by Maiolino et al. (2005); Wang et al. (2013) in the far-infrared. The blue squares are CFHQS quasars at $6.0 < z < 6.4$ published by Willott et al. (2010, 2013, 2015). The black triangles are two $z > 6.5$ quasars previously observed in the far-infrared (published by Venemans et al. 2012 and Bañados et al. 2015). The black hole masses of these two quasars were taken from De Rosa et al. (2014) and Venemans et al. (2015). The green stars are the $6.6 < z < 6.9$ quasars presented in this paper. The black hole masses of these quasars were published in De Rosa et al. (2014). For consistency, L_{FIR} has been computed for all sources assuming $T_d = 47 \text{ K}$ and $\beta = 1.6$.

L_{bol} and L_{FIR} ($L_{[\text{CII}]}$). Although the strong correlation ($r = 0.72$) between L_{bol} and the far-infrared continuum luminosity could suggest that part of the FIR emission is coming from dust heated by the AGN, a similarly strong correlation ($r = 0.67$, or $r = 0.72$ excluding the undetected quasar) can be seen between L_{bol} and $L_{[\text{CII}]}$. Furthermore, the $L_{[\text{CII}]} / L_{\text{FIR}}$ ratio correlates only weakly ($r = -0.38$) with L_{bol} , with quasars occupying a range in $L_{[\text{CII}]} / L_{\text{FIR}}$ at both low and high L_{bol} . By fitting a line through the $L_{[\text{CII}]} - L_{\text{bol}}$ and $\nu L_{\nu, 158 \mu\text{m}} - L_{\text{bol}}$ data, we found the following relations:

$$\nu L_{\nu}(158 \mu\text{m}) = 10^{44.94 \pm 0.15} \left(\frac{L_{\text{bol}}}{10^{13} L_{\odot}} \right)^{1.09 \pm 0.30} L_{\odot}, (2)$$

$$L_{[\text{CII}]} = 10^{9.16 \pm 0.09} \left(\frac{L_{\text{bol}}}{10^{13} L_{\odot}} \right)^{0.68 \pm 0.18} L_{\odot} (3)$$

As mentioned in Section 4.1, a possible explanation for low $L_{[\text{CII}]} / L_{\text{FIR}}$ ratios (the “[C II] deficit”) in quasar hosts is that the strong X-ray radiation from the central AGN reduces the C^+ abundance and hence suppresses the [C II] emission (Langer & Pineda 2015). The positive slope in the $L_{[\text{CII}]} - L_{\text{bol}}$ relation indicates that, in the quasars studied here, this scenario is not the explanation for the [C II] deficit. The positive correlation between the far-infrared continuum and L_{bol} might indicate that a fraction of L_{FIR} could be due to dust heated by the AGN. This is supported by the size estimations of J0305–3150 (Table 2) and of bright quasar hosts at $z \sim 6$ (Wang et al. 2013): the region emitting the continuum radiation seems to be smaller than the [C II] emitting region. However, this does not explain why the [C II] luminosity also correlates with the luminosity of the quasar.

A likely scenario that produces a positive correlation between both $L_{[\text{CII}]} - L_{\text{bol}}$ and $L_{\text{FIR}} - L_{\text{bol}}$ is that a large reservoir of gas is available to both feed the black hole and to form stars. This is in rough agreement with the results of, for example, Leipski et al. (2014) and Barnett et al. (2015) who found that the FIR flux density in $z = 5 - 7$ quasars measured around $160 \mu\text{m}$ is dominated by cold dust emission powered by star formation.

4.3. [C II] vs Mg II Redshifts

As mentioned in Section 3.1, the [C II] emission line did not coincide with the redshift expected from the Mg II line. In one case, J0109–3047, the shift is $\sim 1700 \text{ km s}^{-1}$. Since the Mg II line is originating from the broad line region, its line width is much larger than that of the [C II] line. One question is whether the shifts could be caused by the uncertainty in the determination of the centre of the Mg II line. In Fig. 8 we plotted the (continuum-subtracted) spectra of the quasars around the Mg II line with the best-fit model for the emission line on top (see De Rosa et al. 2014, for the details). In the case of J2348–3054 and J0305–3150, the [C II] line is located relatively close ($< 500 \text{ km s}^{-1}$) to the peak of the Mg II line that in these quasars has a FWHM of $3200 - 5500 \text{ km s}^{-1}$ (De Rosa et al. 2014). On the other hand, the [C II] line in J0109–3047 is clearly at a higher redshift than the peak of the Mg II emission.

These shifts between the Mg II line and the host galaxy redshift as traced by the [C II] line are unexpected, as it has been shown that the Mg II line is a good tracer of the systemic redshift at lower redshifts (e.g., Richards et al. 2002; Hewett & Wild 2010). For example, Richards et al. (2002) studied the SDSS spectra of 417 quasars at $0.415 < z < 0.827$ that contained both the Mg II line and the narrow emission line [O III] $\lambda 5007$ line. They found that the Mg II line has a shift of only $97 \pm 269 \text{ km s}^{-1}$ (see also Fig. 9)¹².

To examine whether the Mg II line in $z \gtrsim 6$ quasar spectra provide a good measure of the systemic redshift, we compiled a list with all quasars at these redshifts that have a redshift measurement from both the Mg II line and a molecular or atomic line (CO or [C II]). We plot the computed velocity shifts from this sample in Fig. 9. The shifts span a large range from $+475 \text{ km s}^{-1}$ (redshift) to -1700 km s^{-1} (blueshift). The mean and the median of this sample are -480 and -467 km s^{-1} , respectively, with a standard deviation of 630 km s^{-1} . The distribution is not centered around 0 km s^{-1} : of the 11 $z \gtrsim 6$ quasars, 8 have a blueshifted Mg II line with respect to the systemic velocity as traced by the molecular or atomic lines. This argues against the scenario in which the shifts are mainly caused by the uncertainties in determining the center of the broad Mg II emission line, although further studies are needed to investigate possible systematics affecting z_{MgII} .

A possible explanation for the large blueshifts is that the broad line region close to the black hole, where the Mg II emission originates, is pushed outwards by the strong radiation of the quasar. We investigated whether there is a correlation between the velocity offset and the Eddington ratio $L_{\text{bol}} / L_{\text{Edd}}$. These two parameters are only marginally correlated ($r = 0.42$). Furthermore, the trend is opposite to our expectations: the quasars with the highest accretion show only small blueshifts, while the object with the largest blueshift, J0109–3047, has a relatively low Eddington ratio of $L_{\text{bol}} / L_{\text{Edd}} \sim 0.2$ (see also De Rosa et al. 2014). Also, no correlation was found between the velocity offset and the bolometric luminosity ($r = 0.03$) and between the offset and the FIR luminosity ($r = -0.02$).

Although our sample is small, the wide distribution of velocity shifts between z_{MgII} and $z_{[\text{CII}]}$ suggest that caution should be taken when using the redshift of the Mg II line as proxy for the systemic redshift. For example, FIR lines may be shifted out of an ALMA bandpass (covering $\sim 2250 \text{ km s}^{-1}$ at 250 GHz), leading to an apparent non-detection.

4.4. Constraints on J0305–3150

The S/N of the observations of J0305–3150 is high enough that we can investigate the properties of this particular source in more detail.

4.4.1. Dynamical Modeling

¹² In general, the [O III] $\lambda 5007$ traces the systemic redshift of quasars very well, with an average shift between the [O III] line and the systemic redshift of $40 - 45 \text{ km s}^{-1}$ (e.g., Boroson 2005; Hewett & Wild 2010). However, in some cases the [O III] line can display large offsets of up to 400 km s^{-1} , especially in quasars with a high accretion rate (e.g., Boroson 2005; Bae & Woo 2014).

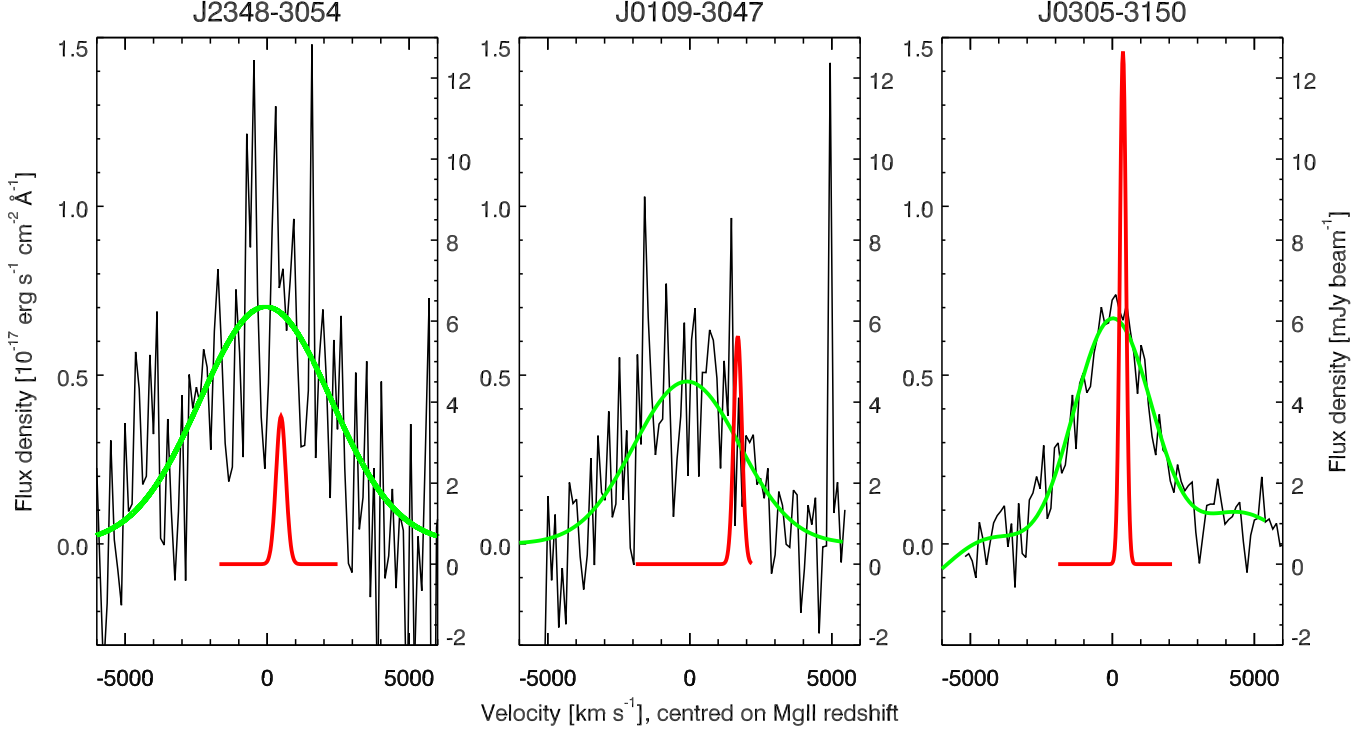


Figure 8. Continuum subtracted near-infrared spectra around the Mg II emission line of the three quasars (black thin lines) with the model of the Mg II emission line overplotted in green (taken from Fig. 4 of De Rosa et al. 2014). In red the Gaussian fits to the [C II] emission line (see Fig. 1) are shown. The left y-axis gives the flux units of the Mg II line, whereas the right y-axis gives the units of the [C II] line emission. On the x-axis we plot the velocity with respect to the Mg II redshift. In particular in the case of J0109-3047, the peak of the Mg II and [C II] lines show significant offsets from each other (see discussion in Section 4.3).

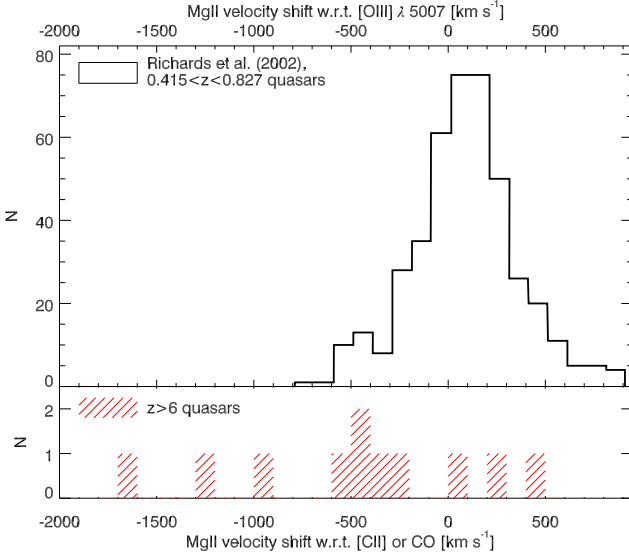


Figure 9. *Top:* Histogram showing the distribution of the velocity shift of the Mg II emission line center with respect to that of the [O III] λ 5007 line of 417 quasars at $0.415 < z < 0.827$ (from Richards et al. 2002). Negative velocities indicate a blueshift of the Mg II line compared to the [O III] line. *Bottom:* In the red hashed histogram we plot the velocity shift between the redshift determined from the Mg II line and that of the quasar host galaxy traced by [C II] or CO emission of $z > 6$ quasars. While in low redshift quasar spectra the Mg II line is redshifted, on average, by $97 \pm 269 \text{ km s}^{-1}$ (Richards et al. 2002), at $z > 6$ the Mg II line is predominantly blueshifted with respect to the host galaxy redshift with a mean and standard deviation of $-480 \pm 630 \text{ km s}^{-1}$.

From Fig. 4 it is clear that the red and blue side of the emission line in J0305-3150 are displaced from each other. This is an indication that ordered motion is present in this quasar host, and it is possible that the gas is located in a rotating disk. In contrast to the other two quasar hosts, the [C II] line in J0305-3150 has been detected at high enough S/N ($S/N > 25$) to permit modeling of the gas emission.

Empirical tilted-ring models were created to match the data using the Tilted Ring Fitting Code (TiRiFiC, Józsa et al. 2007). These models include a single disk component of constant scale height. Our data clearly rule out models with a constant surface brightness and a constant rotation velocity (here set to 150 km s^{-1} , see Fig. 10). A decreasing surface brightness distribution allowed for an improved fit to the data, followed by the addition of a linearly increasing rotation curve (starting at 0 km s^{-1} and peaking at 150 km s^{-1} at $0''.1$ (which corresponds to 0.55 kpc at $z = 6.6415$) before remaining constant for larger radii), which improved the fit substantially. Although the resolution is poor, from these models it is clear that we can rule out a flat rotation curve and that the rotation curve is increasing instead. However, from the final two panels of Fig. 10, it is seen that the inclination cannot be well constrained at our current resolution. If the gas in this quasar host galaxy is distributed in a disk, we only observe the rising part of the rotation curve. In other words, with the current data we cannot independently determine the inclination angle and the peak velocity and thus, ultimately, the dynamical mass. We will estimate a dynamical mass from the

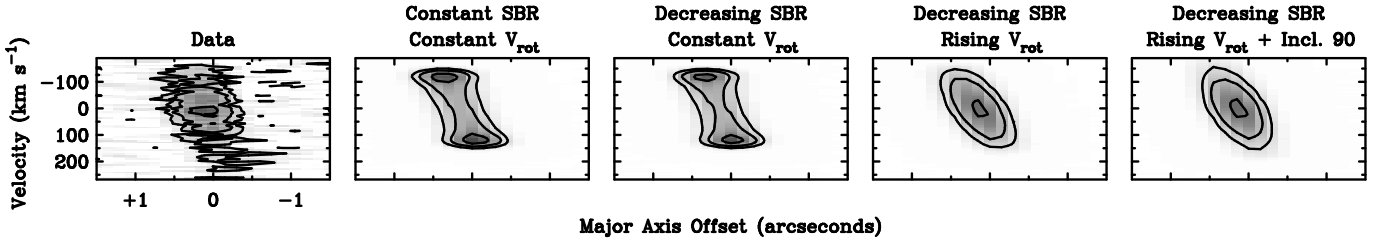


Figure 10. Major axis position-velocity diagrams of the data, compared with simple theoretical models convolved to our instrumental resolution. The models are: a model with both constant surface brightness and rotational velocity with radius, a model with a constant rotational velocity of 150 km s^{-1} with decreasing surface brightness, a model with decreasing surface brightness and rising rotation curve (from 0 to 150 km s^{-1} at $0''.1$, which corresponds to 0.55 kpc at $z = 6.6145$), and a model with decreasing surface brightness, rising rotation curve (from 0 to 180 km s^{-1} at $0''.1$), and an inclination of 90° . All other model inclinations are 60° . Note that a rising rotation curve is clearly necessary to provide a match to the data, but at the current resolution there is a degeneracy between inclinations, and thus the intrinsic rotation speed.

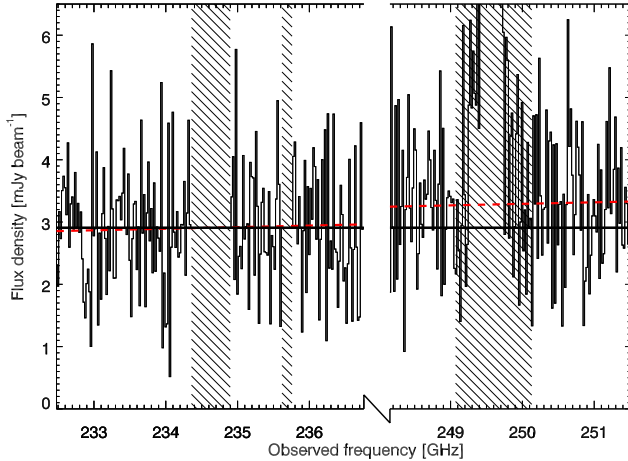


Figure 11. Spectrum extracted at the brightest pixel in the data cube of J0305–3150 smoothed with a $1''$ Gaussian, binned over 20 MHz. The hashed regions (containing a gap in the frequency coverage and the [C II] line) are not used when computing the continuum flux density. The black solid line shows the average continuum flux density measured between 232.5 GHz and 236.7 GHz. An increase of the continuum flux density is clearly apparent over the frequency range covered by our observations. The continuum near the [C II] line (redshifted to 249.6 GHz) is $\sim 16\%$ higher. The red, dashed line shows the best fitting modified black body.

observed line width for this and the other two quasar hosts in Section 4.6.

4.4.2. Additional Emission Components

The high S/N of the [C II] line in J0305–3150 enables us to search for emission that deviates from the Gaussian fit. From the spectrum in Fig. 1 we identified highly significant ($\sim 7\sigma$) excess emission on the red side (low frequency side) of the Gaussian emission line. The map of this excess emission is shown in Fig. 4 as green contours. The flux density of this excess emission above the Gaussian fit is $1.69 \pm 0.23 \text{ mJy}$. The location of this emission is significantly offset from the central line emission by $0''.41 \pm 0''.04$ ($2.3 \pm 0.2 \text{ kpc}$). Similarly blueshifted emission is not seen on the other side of the [C II] line. The origin of this second component is unclear: it could be an outflow, inflowing gas, or a close companion to the quasar. Higher S/N and/or higher spatial resolution will help to distinguish these different cases.

4.4.3. Continuum Slope

The frequency setup of the ALMA observations allows us to measure the dust continuum in the quasar host

around two frequencies that are roughly 15 GHz apart. For a source at $z = 6.6$, this is $\sim 115 \text{ GHz}$ in the rest-frame. Over this large frequency range the dust continuum is not constant. In Fig. 11 we plot the spectrum of J0305–3150 in all four bandpasses. The higher frequency data cube was smoothed with a $1''$ Gaussian and the extracted spectrum (between 248.1 and 251.5 GHz) is identical to the spectrum shown in Fig. 1. Because the source is resolved (Table 2) and the resolution of the data changes over the frequency range probed by the observations, we smoothed the lower frequency data to match the resolution of the (smoothed) higher frequency data. The average continuum level in the observed frequency range 232.5–236.7 GHz is $2.91 \pm 0.07 \text{ mJy}$. If we exclude a region of $\sim 1.0 \text{ GHz}$ ($5\times$ the FWHM of the [C II] line) wide around the [C II] line, we measure an average continuum level of $3.29 \pm 0.10 \text{ mJy}$ around 250 GHz. The continuum flux density around 250 GHz is $0.38 \pm 0.12 \text{ mJy}$ higher than around 234 GHz, a difference of 3.1σ . Assuming that this difference is caused by the shape of the dust continuum emission, we can put constraints the temperature of the dust. Fitting a modified black body with a fixed $\beta = 1.6$ to the continuum spectrum shown in Fig. 11 results in a best-fitting temperature of $T_d = 37^{+11}_{-7} \text{ K}$. We estimated the uncertainty in the temperature by randomly adding noise to the spectrum and remeasuring the best-fitting dust temperature 10,000 times. For the 1σ uncertainties we took the range of temperatures of 68% of the values around the median. Since we are in the Rayleigh-Jeans tail of the modified black body, the uncertainties are asymmetric and non-Gaussian. The 95% range (2σ) of the best-fitting dust temperature is 25–74 K. Since the dust temperature we derive from fitting the continuum is only 16 K above the CMB temperature at this redshift, $T_{\text{CMB}}(z = 6.61) = 20.8 \text{ K}$, we consider the effects of the CMB on the observed dust emission in the next section.

4.5. Effects of the Cosmic Microwave Background

The effects of the CMB on millimeter observations of high redshift galaxies are extensively discussed in da Cunha et al. (2013). To summarize, when the CMB temperature is close to the temperature of the dust in a high redshift galaxy, there are two competing processes that impact the observed mm luminosity of the galaxy. Firstly, the CMB supplies an additional source that heats the dust. The higher dust temperature can be calculated with the following formula from da Cunha et al. (2013):

$$T_d(z) = [(T_d^{z=0})^{4+\beta} + (T_{\text{CMB}}^{z=0})^{4+\beta} \times ((1+z)^{4+\beta} - 1)]^{\frac{1}{4+\beta}}, \quad (4)$$

where $T_d^{z=0}$ is the dust temperature ignoring heating by the CMB and $T_{\text{CMB}}^{z=0}$ is the CMB temperature at $z = 0$. The increase in dust temperature due to heating by the CMB is negligible for $T_d = 47$ K and $\beta = 1.6$ that we assumed in Section 3. If the dust temperature is 30 K (within 1σ of our best-fitting temperature for J0305–3150, see Section 4.4.3), the CMB increases the dust temperature by $\sim 2\%$ at $z = 6.6$.

The second effect of the CMB on our observations is that it reduces the detectability of the dust continuum. The fraction of the flux density that we measure against the CMB is:

$$f_\nu^{\text{obs}}/f_\nu^{\text{intrinsic}} = 1 - B_\nu(T_{\text{CMB}}(z))/B_\nu(T_d(z)), \quad (5)$$

with B_ν the Planck function at rest-frame frequency ν (da Cunha et al. 2013). At $z = 6.6$, this correction factor at a rest-frame wavelength of $158 \mu\text{m}$ is close to unity (~ 0.92) for a dust temperature of $T_d = 47$ K. If we again assume a dust temperature of $T_d = 30$ K instead of 47 K, we already miss $\sim 25\%$ of the intrinsic flux density due to the CMB background emission. The fraction of the flux density that we can measure against the CMB also depends on the frequency and thus affects the continuum slope that we measure.

In Section 4.4.3 we fitted the continuum emission of J0305–3150 with a modified black body and derived a best-fitting temperature in the range $T_d = 30 - 48$ K. If the true dust temperature in the quasar host is in the upper end of this range, then the effects of the CMB on our observations will be negligible, as we have described above. On the other hand, in the case that the temperature of the dust in J0305–3150 is closer to 30 K, the CMB will have a non-negligible influence on the dust properties we derive from fitting the continuum spectrum as shown in Figure 11.

As a test, we therefore fitted the continuum spectrum of J0305–3150 again, this time fitting a modified black body while taking the effects of the CMB into account: the dust temperature was modified according to Equation 4 and the resulting flux density was adjusted using Equation 5. With a fixed $\beta = 1.6$ and redshift $z = 6.6145$ (Table 2), we measure a lower intrinsic dust temperature of $T_d^{z=0} = 30$ K, with a 1σ range of 21–42 K. Although the dust heating due to the CMB is negligible ($\sim 2\%$ temperature increase) for this source if $T_d^{z=0} = 30$ K, observing against the CMB background reduces the flux density we are measuring to approximately 77% of the intrinsic flux density.

Although our error bars are large, the lower dust temperature derived from the continuum slope suggests that we may have overestimated the infrared luminosity of this quasar host by assuming $T_d = 47$ K. Using $T_d = 30$ K, $\beta = 1.6$ and taking into account that the intrinsic flux density is a factor $1/0.77 = 1.3$ higher than the observed flux density, we derived an intrinsic $L_{\text{FIR}} = 2.6 \times 10^{12} L_\odot$, which is below the range of L_{FIR} we estimated for this quasar host ($(4.0 - 7.5) \times 10^{12} L_\odot$, see Section 3.4 and Table 2). The total infrared luminosity L_{TIR} would also be below our previous estimates: $L_{\text{TIR}} = 3.7 \times 10^{12} L_\odot$, implying, if powered by star formation, a $\text{SFR}_{\text{TIR}} = 545 M_\odot \text{yr}^{-1}$. We note that we have fixed β here; to further constrain the shape and lumi-

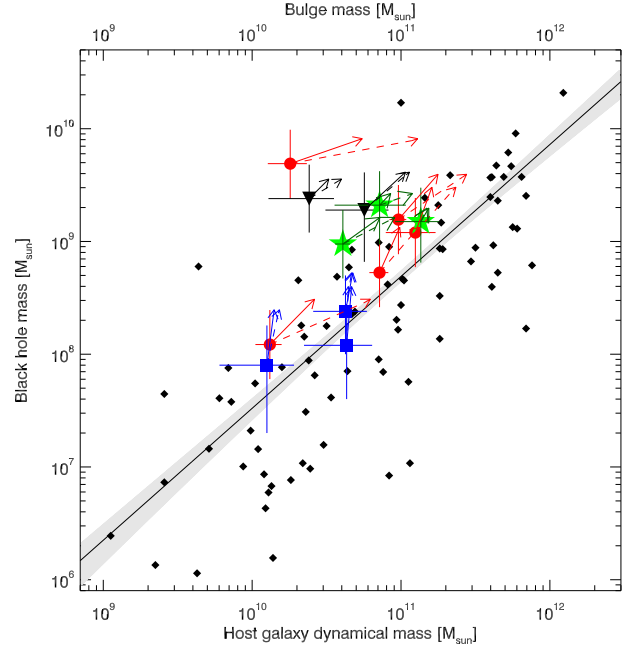


Figure 12. Black hole mass plotted against the dynamical mass of $z \gtrsim 6$ quasar host galaxies and the bulge mass of local galaxies. The black diamonds are values obtained for local galaxies (taken from Kormendy & Ho 2013). The solid line and the shaded area shows the local $M_{\text{BH}}-M_{\text{bulge}}$ relation derived by Kormendy & Ho (2013). Values for $z \gtrsim 6$ quasar hosts are plotted in the same colored symbols as in Fig. 5. Following Willott et al. (2015), we added 0.3 dex in quadrature to the errors to include the systematic uncertainty in deriving a black hole from local scaling relations. The values of the dynamical mass for the $z < 6.5$ quasar hosts are taken from Willott et al. (2015). The green stars are the $z > 6.5$ quasars presented in this work. For a given bulge mass, the high redshift quasars have a more massive black than local galaxies. The arrows indicate the black hole mass and galaxy mass of the quasar hosts if the measured black hole growth and SFR continue for the next 50 Myr. The solid lines show the galaxy mass growth using the [C II]-derived SFR, while the dashed lines use the L_{TIR} SFR estimates.

nosity of the far-infrared continuum and the properties of the dust, we require additional photometry at different frequencies (for example, continuum measurements in other ALMA bands).

4.6. Dynamical mass estimates

A procedure often applied in the literature to compute the dynamical mass M_{dyn} in quasar hosts is to use the line width and spatial extent of the emission (e.g., Walter et al. 2003; Wang et al. 2013; Willott et al. 2015): $M_{\text{dyn}} = 1.16 \times 10^5 v_{\text{circ}}^2 D M_\odot$, where v_{circ} is the circular velocity in km s^{-1} and D the diameter of the gas disk in kpc. Following Wang et al. (2013) we assume that the gas is distributed in an inclined disk and the circular velocity is given by $v_{\text{circ}} = 0.75 \text{FWHM}/\sin(i)$ (e.g., Ho 2007) with i the inclination angle. The inclination angle can be derived from the observed minor to major axis ratio: $i = \cos^{-1}(a_{\text{min}}/a_{\text{maj}})$, assuming a thin disk geometry. For J0109–3047 and J0305–3150 we (marginally) resolve the [C II] emitting region and we derive an inclination angle of 25° and 50° , respectively. For J2348–3054, we assume the inclination angle is similar to that of other $z \gtrsim 6$ quasar hosts, which have a median inclination angle of $i = 55^\circ$ (Wang et al. 2013). The diameter D is set to $1.5 \times$ the deconvolved size of the [C II] emitting re-

gion (Wang et al. 2013, see Table 2). For the unresolved emission in the host of J2348–3054 we assume an extent of 3 ± 1 kpc. With these numbers, we calculate a dynamical mass of $(7.2 \pm 3.6) \times 10^{10} M_{\odot}$, $(1.4 \pm 0.4) \times 10^{11} M_{\odot}$, and $(4.1 \pm 0.5) \times 10^{10} M_{\odot}$ for J2348–3054, J0109–3047, and J0305–3150, respectively. The uncertainty in these dynamical masses does not include the uncertainties in the inclination angle.

The dynamical galaxy mass we derived for each of the quasar hosts is the sum of all the mass inside the central few kpc of the galaxies. There are various galaxy components that contribute to this mass: the central black hole, stars, dust and gas, and dark matter. While the black hole contributes only a small fraction to the dynamical mass, the gas can provide a significant fraction of the mass. If we take the local gas-to-dust mass ratio of ~ 100 (e.g., Draine et al. 2007), the derived dust masses in our quasar hosts of $M_d = (1-24) \times 10^8 M_{\odot}$ imply gas masses of $M_g = (1-24) \times 10^{10} M_{\odot}$. In some cases, this is a significant fraction of the computed dynamical mass for these objects. If we assume the extreme case that the dynamical mass is all in the form of stars in a bulge, we get an upper limit on the bulge mass in these quasar hosts. In Fig. 12, we show M_{BH} as function of M_{dyn} . We also plotted the values of the black hole mass and bulge mass for local galaxies, which follow the relation: $M_{\text{BH}}/10^9 M_{\odot} = (0.49^{+0.06}_{-0.05})(M_{\text{bulge}}/10^{11} M_{\odot})^{1.17 \pm 0.08}$ (Kormendy & Ho 2013). All but one of the $z \gtrsim 6$ quasar hosts are laying above the local relation. In other words, for a given bulge (or dynamical) mass, the black holes in the high redshift quasar hosts are more massive than those of local galaxies. Since the true stellar bulge masses in the quasar hosts are likely lower than M_{dyn} , the offsets only get more extreme. Fixing the slope of 1.17 in the black hole–bulge mass relation, we computed the average ratio of $M_{\text{BH}}/M_{\text{dyn}}$ at a galaxy mass of $10^{11} M_{\odot}$ for the quasar hosts at $z \gtrsim 6$. We find a mean of 1.9% and a median of 1.3%, compared to the local value of $0.49^{+0.06}_{-0.05}\%$. This is a factor ~ 3 –4 higher, in agreement with studies of the host of quasars at $z \gtrsim 2$ (e.g., McLure et al. 2006; Peng et al. 2006; Shields et al. 2006; Decarli et al. 2010; Merloni et al. 2010; Targett et al. 2012). If we parametrize the redshift evolution of the black hole–bulge mass relation as $M_{\text{BH}}/M_{\text{bulge}} = (M_{\text{BH}}/M_{\text{bulge}})_{z=0} \times (1+z)^{\beta}$ (e.g., McLure et al. 2006; Merloni et al. 2010; Bennert et al. 2011; Targett et al. 2012), then we find for the $z \gtrsim 6$ quasar hosts a mean of $\beta = 0.7$ and a median of $\beta = 0.5$, again in agreement with the literature.

We also investigated the $M_{\text{BH}} - \sigma$ relation by computing the velocity dispersion σ from the circular velocity: $\log(v_{\text{circ}}) = (0.84 \pm 0.09)\log(\sigma) + (0.55 \pm 0.19)$ (Ferrarese 2002). However, it remains unclear whether this relation between v_{circ} and σ can be applied here as Kormendy & Ho (2013) argue that the tight correlation between these parameter might only be valid for galaxies that contain an actual bulge (which is unknown in these quasar hosts). Nevertheless, the $z \gtrsim 6$ data point are on average above the local $M_{\text{BH}} - \sigma$ relation, similar to the points in Fig. 12. If we calculate the dispersion by simply converting the FWHM of the Gaussian [C II] line to a σ ($\sigma = \text{FWHM} / (2\sqrt{2\ln(2)})$), the σ of the quasar hosts are smaller than those computed from v_{circ} , and the points

are even further away from the local relation.

Finally, we can estimate in which directions the points in Fig. 12 are moving with cosmic time. This would address the question whether, over time, the star formation rates measured in the distant quasar hosts will move the host galaxies on the local $M_{\text{BH}} - M_{\text{bulge}}$ relation. From the bolometric luminosity of the quasar (see Section 4.2 and Equation 1), we can compute the growth of the black hole \dot{M}_{BH} : $\dot{M}_{\text{BH}} = \frac{1-\eta}{\eta} \frac{L_{\text{bol}}}{c^2}$ (Barnett et al. 2015), with η the radiative efficiency ($\eta \approx 0.07$, Volonteri & Rees 2005). For example, for the VIKING quasars we derive a black hole growth of 11, 10, and $14 M_{\odot} \text{yr}^{-1}$, for J2348–3054, J0109–3047, and J0305–3150, respectively. When compared to the SFRs of 270, 355, and $630 M_{\odot} \text{yr}^{-1}$ derived from the [C II] line (Section 3), the black hole is growing at a rate of 2–4% of the SFR. Since these quasar hosts already have a higher black hole to bulge mass ratio than the local value of 0.49%, this high growth ratio means that the quasar hosts will not move towards the local relation over time (assuming that the accretion/growth rates do not change). Similarly, if we assume that the galaxies are growing with SFRs derived from L_{TIR} (~ 950 , 270, and $540 M_{\odot} \text{yr}^{-1}$ for J2348–3054, J0109–3047, and J0305–3150, respectively, see Sections 3.2, 3.3, and 4.5), the black holes are growing at a rate of 1–4% of the SFR.

In Fig. 12, we show the direction of the relative growth of black hole and galaxy mass in a time span of 50 Myr for the $z \gtrsim 6$ quasar hosts with respect to the local black hole–bulge mass relation. The black hole growth was computed using the bolometric luminosity of the central AGN. The galaxy growth was calculated using either $\text{SFR}_{[\text{CII}]}$ (solid lines) or SFR_{TIR} (dashed lines), with the assumption that all the far-infrared emission arises from star formation and that the material forming the new stars is accreted onto the galaxy (i.e., that the dynamical mass were to increase by that amount). If we assume that the SFR is traced by the [C II] emission, then for the majority of quasar hosts, especially the ones close to the local $M_{\text{BH}} - M_{\text{bulge}}$ relation, the black hole is growing faster than the host galaxies: on average, in 50 Myr the black hole increases its mass by a factor ~ 2.2 , while the host galaxy grows by a factor 1.35–1.55 in mass. The $M_{\text{BH}}/M_{\text{dyn}}$ ratio for the quasar hosts will therefore have increased after 50 Myr from 1.3–1.9% to 2.0–2.5%. It is possible, however, that by using the [C II] luminosity, we underestimated the SFR, especially in the quasar hosts with low $L_{[\text{CII}]} / L_{\text{FIR}}$ ratios (e.g., De Looze et al. 2014). Taking instead the TIR luminosity to derive SFRs (which could overestimate the SFR, see e.g., Section 4.2), the galaxies grow by a factor of 1.7–2.3 in 50 Myr and as a result the black hole to bulge mass ratio will be similar at 1.3–1.9%. Even with the larger SFR_{TIR} the vast majority (if not all) of the quasar hosts will lie above the local relation.

5. SUMMARY

In this paper we presented short (~ 15 min) ALMA observations of three quasars at $z > 6.6$: J0305–3150 at $z = 6.61$, J0109–3047 at $z = 6.75$, and J2348–3054 at $z = 6.89$. All three quasars have been detected in the [C II] emission line and in the underlying, far-infrared continuum at high significance.

- We measure [C II] line fluxes between $1.6\text{--}3.4\text{ Jy km s}^{-1}$, which corresponds to [C II] luminosities of $L_{\text{[CII]}} = (1.9\text{--}3.9) \times 10^9 L_{\odot}$. This is 2–3 times brighter than the [C II] line in the most distant quasar known, ULAS J1120+0641 at $z = 7.1$, but fainter than the [C II] line in P036+03 at $z = 6.5$ (Bañados et al. 2015). The [C II] line width are $255, 340$, and 405 km s^{-1} , very similar to that of other $z \gtrsim 6$ quasar hosts (e.g., Wang et al. 2013; Willott et al. 2015). For two sources, J0109–3047 and J0305–3150, we resolved the [C II] line emission and we derive sizes $2\text{--}3\text{ kpc}$, which is again similar to the sizes of [C II] emitting regions in $z \sim 6$ quasar hosts (Walter et al. 2009; Wang et al. 2013; Willott et al. 2013, 2015). By modeling the brightest of our detected [C II] emission lines with disk models, we can rule out that the gas has a flat rotation curve.
- From the line free channels we obtain continuum flux densities of $0.56\text{--}3.29\text{ mJy}$ around $158\text{ }\mu\text{m}$ (rest-frame). Depending on the shape of the dust continuum, the far-infrared luminosity of the quasar hosts is $L_{\text{FIR}} = (0.6\text{--}7.5) \times 10^{12} L_{\odot}$. The total infrared luminosities are $(0.9\text{--}10.6) \times 10^{12} L_{\odot}$ and we derive dust masses between $(0.7\text{--}24) \times 10^8 M_{\odot}$. Only in the case of J0305–3150, the quasar host with the brightest continuum emission, we spatially resolve the continuum emission, with a deconvolved continuum size that is smaller than the size of the [C II] emitting region in the same object.
- We fitted the slope of the FIR continuum in J0305–3150 to put a constraint on the dust temperature. After taking the effects of the CMB into account, we derive a dust temperature of $T_d = 30^{+12}_{-9}\text{ K}$. This is lower than the canonical value of $T_d = 47\text{ K}$ assumed for distant quasar hosts. The FIR luminosity implied by a dust temperature of $T_d = 30\text{ K}$ is a factor ~ 3 lower compared to L_{FIR} computed using $T_d = 47\text{ K}$, illustrating that caution has to be taken when deriving FIR and TIR luminosities from single continuum measurements of distant quasar hosts.
- The [C II] equivalent widths are $0.43, 1.90$, and $0.55\text{ }\mu\text{m}$, for J2348–3054, J0109–3047, and J0305–3150, respectively. These values are at most a factor of 3 below that of local starburst galaxies which have a median $\text{EW}_{\text{[CII]}} = 1.3\text{ }\mu\text{m}$ (Díaz-Santos et al. 2013; Sargsyan et al. 2014). Depending on the shape of the FIR continuum, the $L_{\text{[CII]}}/L_{\text{FIR}}$ range from $(0.3\text{--}4.6) \times 10^{-3}$. J0109–3047 has a ratio of $(1.4\text{--}4.6) \times 10^{-3}$, consistent with local star-forming galaxies. The other two quasar hosts have low values, $(0.3\text{--}1.0) \times 10^{-3}$, similar to FIR bright quasar hosts at $z \sim 6$ (Wang et al. 2013).
- If the [C II] and continuum emission are powered by star formation, we find star-formation rates from $140\text{--}895 M_{\odot}\text{ yr}^{-1}$ for J0109–3047, based on local scaling relations. For the other two sources we derive SFRs from $L_{\text{[CII]}}$ between $100\text{--}1585 M_{\odot}\text{ yr}^{-1}$ and $\text{SFR}_{\text{TIR}} = 555\text{--}1580 M_{\odot}\text{ yr}^{-1}$.
- We combined our results with those of $z \gtrsim 6$ quasars with [C II] measurements in the literature. We find that the strength of the $L_{\text{[CII]}}$ and L_{FIR} emission both correlate with the bolometric luminosity L_{bol} of the quasar. The $L_{\text{[CII]}}/L_{\text{FIR}}$ ratio only weakly correlates with L_{bol} , implying that low $L_{\text{[CII]}}/L_{\text{FIR}}$ ratios in quasar hosts are not mainly due to high L_{FIR} due to quasar heating of the dust.
- The [C II] line in J0109–3047 is shifted by 1700 km s^{-1} with respect to the Mg II line that was used to tune the ALMA observations. We compared the redshifts of 11 $z \gtrsim 6$ quasars based on the Mg II line, coming from the quasar broad line region, with the host galaxy redshifts traced by [C II] or CO. Of these 11 quasars, 8 have a blueshifted Mg II line with respect to the host galaxy redshift. The average blueshift of the sample is $480 \pm 630\text{ km s}^{-1}$. The Mg II shifts are uncorrelated with the luminosity and accretion rate of the central AGN, and with the host galaxy brightness.
- Finally, we derived dynamical masses for the quasar hosts from the observed [C II] line width and spatial extent. We find that the ratio of black hole mass to host galaxy mass is higher by a factor 3–4 than local relations. We find that the black hole to galaxy mass ratio evolves as $(1+z)^{0.5-0.7}$, indicating that black holes grow faster than their host galaxies in the early universe for the quasars considered here. This is supported by the relative growth rates: we computed the growth rate of the black holes (derived from the quasar’s bolometric luminosities) and that of the host galaxies (based on the measured SFRs) and, on average, the black holes are growing at least as fast as their host galaxies.

We thank the referee for carefully reading the manuscript and providing valuable comments and suggestions. B.P.V. and F.W. acknowledge funding through the ERC grant “Cosmic Dawn”. Support for R.D. was provided by the DFG priority program 1573 “The physics of the interstellar medium”.

This paper makes use of the following ALMA data: ADS/JAO.ALMA#2012.1.00882.S. ALMA is a partnership of ESO (representing its member states), NSF (USA) and NINS (Japan), together with NRC (Canada) and NSC and ASIAA (Taiwan), in cooperation with the Republic of Chile. The Joint ALMA Observatory is operated by ESO, AUI/NRAO and NAOJ.

This publication makes use of data products from the *Wide-field Infrared Survey Explorer*, a joint project of the University of California, Los Angeles, and the Jet Propulsion Laboratory/ California Institute of Technology, funded by the National Aeronautics and Space Administration.

Facilities: ALMA.

REFERENCES

- Bañados, E., Decarli, R., Walter, F., et al. 2015, *ApJL*, 805, L8
- Bae, H.-J., & Woo, J.-H. 2014, *ApJ*, 795, 30
- Barnett, R., Warren, S. J., Banerji, M., et al. 2015, *A&A*, 575, A31
- Beelen, A., Cox, P., Benford, D. J., et al. 2006, *ApJ*, 642, 694
- Bennert, V. N., Auger, M. W., Treu, T., Woo, J.-H., & Malkan, M. A. 2011, *ApJ*, 742, 107
- Bertoldi, F., Carilli, C. L., Cox, P., et al. 2003a, *A&A*, 406, L55
- Bertoldi, F., Cox, P., Neri, R., et al. 2003b, *A&A*, 409, L47
- Boroson, T. 2005, *AJ*, 130, 381
- Brisbin, D., Ferkinhoff, C., Nikola, T., et al. 2015, *ApJ*, 799, 13
- Cai, Z.-Y., Lapi, A., Xia, J.-Q., et al. 2013, *ApJ*, 768, 21
- Calura, F., Gilli, R., Vignali, C., et al. 2014, *MNRAS*, 438, 2765
- Carniani, S., Maiolino, R., De Zotti, G., et al. 2015, *ArXiv e-prints*, arXiv:1502.00640
- Cox, P., Krips, M., Neri, R., et al. 2011, *ApJ*, 740, 63
- da Cunha, E., Groves, B., Walter, F., et al. 2013, *ApJ*, 766, 13
- De Breuck, C., Maiolino, R., Caselli, P., et al. 2011, *A&A*, 530, L8
- De Breuck, C., Seymour, N., Stern, D., et al. 2010, *ApJ*, 725, 36
- de Looze, I., Baes, M., Bendo, G. J., Cortese, L., & Fritz, J. 2011, *MNRAS*, 1090
- De Looze, I., Cormier, D., Lebouteiller, V., et al. 2014, *A&A*, 568, A62
- De Rosa, G., Decarli, R., Walter, F., et al. 2011, *ApJ*, 739, 56
- De Rosa, G., Venemans, B. P., Decarli, R., et al. 2014, *ApJ*, 790, 145
- Decarli, R., Falomo, R., Treves, A., et al. 2010, *MNRAS*, 402, 2453
- Díaz-Santos, T., Armus, L., Charmandaris, V., et al. 2013, *ApJ*, 774, 68
- Draine, B. T., Dale, D. A., Bendo, G., et al. 2007, *ApJ*, 663, 866
- Dunne, L., Eales, S., Edmunds, M., et al. 2000, *MNRAS*, 315, 115
- Fan, X., Strauss, M. A., Schneider, D. P., et al. 2003, *AJ*, 125, 1649
- Fan, X., Strauss, M. A., Becker, R. H., et al. 2006, *AJ*, 132, 117
- Farrah, D., Lebouteiller, V., Spoon, H. W. W., et al. 2013, *ApJ*, 776, 38
- Ferrarese, L. 2002, *ApJ*, 578, 90
- Gall, C., Hjorth, J., & Andersen, A. C. 2011, *A&AR*, 19, 43
- Gehrels, N. 1986, *ApJ*, 303, 336
- Gullberg, B., De Breuck, C., Vieira, J. D., et al. 2015, *MNRAS*, 449, 2883
- Helou, G., Khan, I. R., Malek, L., & Boehmer, L. 1988, *ApJS*, 68, 151
- Herrera-Camus, R., Bolatto, A. D., Wolfire, M. G., et al. 2015, *ApJ*, 800, 1
- Hewett, P. C., & Wild, V. 2010, *MNRAS*, 405, 2302
- Ho, L. C. 2007, *ApJ*, 669, 821
- Iverson, R. J., Swinbank, A. M., Swinyard, B., et al. 2010, *A&A*, 518, L35
- Jiang, L., Fan, X., Vestergaard, M., et al. 2007, *AJ*, 134, 1150
- Józsa, G. I. G., Kenn, F., Klein, U., & Oosterloo, T. A. 2007, *A&A*, 468, 731
- Komatsu, E., Smith, K. M., Dunkley, J., et al. 2011, *ApJS*, 192, 18
- Kormendy, J., & Ho, L. C. 2013, *ARA&A*, 51, 511
- Kroupa, P., & Weidner, C. 2003, *ApJ*, 598, 1076
- Kuo, T.-M., & Hirashita, H. 2012, *MNRAS*, 424, L34
- Kurk, J. D., Walter, F., Fan, X., et al. 2007, *ApJ*, 669, 32
- Langer, W. D., & Pineda, J. L. 2015, *A&A*, 580, A5
- Leipski, C., Meisenheimer, K., Walter, F., et al. 2013, *ApJ*, 772, 103
- . 2014, *ApJ*, 785, 154
- Madau, P., & Dickinson, M. 2014, *ARA&A*, 52, 415
- Maiolino, R., Caselli, P., Nagao, T., et al. 2009, *A&A*, 500, L1
- Maiolino, R., Schneider, R., Oliva, E., et al. 2004, *Nature*, 431, 533
- Maiolino, R., Cox, P., Caselli, P., et al. 2005, *A&A*, 440, L51
- Malhotra, S., Kaufman, M. J., Hollenbach, D., et al. 2001, *ApJ*, 561, 766
- McLure, R. J., Jarvis, M. J., Targett, T. A., Dunlop, J. S., & Best, P. N. 2006, *MNRAS*, 368, 1395
- Merloni, A., Bongiorno, A., Bolzonella, M., et al. 2010, *ApJ*, 708, 137
- Michałowski, M. J., Murphy, E. J., Hjorth, J., et al. 2010, *A&A*, 522, A15
- Mor, R., Netzer, H., Trakhtenbrot, B., Shemmer, O., & Lira, P. 2012, *ApJL*, 749, L25
- Mortlock, D. J., Warren, S. J., Venemans, B. P., et al. 2011, *Nature*, 474, 616
- Murphy, E. J., Condon, J. J., Schinnerer, E., et al. 2011, *ApJ*, 737, 67
- Peng, C. Y., Impey, C. D., Rix, H.-W., et al. 2006, *ApJ*, 649, 616
- Rangwala, N., Maloney, P. R., Glenn, J., et al. 2011, *ApJ*, 743, 94
- Richards, G. T., Vanden Berk, D. E., Reichard, T. A., et al. 2002, *AJ*, 124, 1
- Richards, G. T., Lacy, M., Storrie-Lombardi, L. J., et al. 2006, *ApJS*, 166, 470
- Riechers, D. A., Carilli, C. L., Capak, P. L., et al. 2014, *ApJ*, 796, 84
- Robertson, B. E., Ellis, R. S., Dunlop, J. S., McLure, R. J., & Stark, D. P. 2010, *Nature*, 468, 49
- Runnoe, J. C., Brotherton, M. S., & Shang, Z. 2012, *MNRAS*, 422, 478
- Sargsyan, L., Samsonyan, A., Lebouteiller, V., et al. 2014, *ApJ*, 790, 15
- Sargsyan, L., Lebouteiller, V., Weedman, D., et al. 2012, *ApJ*, 755, 171
- Seymour, N., Stern, D., De Breuck, C., et al. 2007, *ApJS*, 171, 353
- Shields, G. A., Menezes, K. L., Massart, C. A., & Vanden Bout, P. 2006, *ApJ*, 641, 683
- Shimizu, I., Yoshida, N., & Okamoto, T. 2012, *MNRAS*, 427, 2866
- Silva, L., Granato, G. L., Bressan, A., & Danese, L. 1998, *ApJ*, 509, 103
- Stacey, G. J., Hailey-Dunsheath, S., Ferkinhoff, C., et al. 2010, *ApJ*, 724, 957
- Targett, T. A., Dunlop, J. S., & McLure, R. J. 2012, *MNRAS*, 420, 3621
- Valiante, R., Schneider, R., Salvadori, S., & Gallerani, S. 2014, *MNRAS*, 444, 2442
- Venemans, B. P., McMahon, R. G., Walter, F., et al. 2012, *ApJL*, 751, L25
- Venemans, B. P., Findlay, J. R., Sutherland, W. J., et al. 2013, *ApJ*, 779, 24
- Venemans, B. P., Bañados, E., Decarli, R., et al. 2015, *ApJL*, 801, L11
- Volonteri, M., & Rees, M. J. 2005, *ApJ*, 633, 624
- Wagg, J., Carilli, C. L., Wilner, D. J., et al. 2010, *A&A*, 519, L1
- Walter, F., Riechers, D., Cox, P., et al. 2009, *Nature*, 457, 699
- Walter, F., Bertoldi, F., Carilli, C., et al. 2003, *Nature*, 424, 406
- Wang, R., Carilli, C. L., Wagg, J., et al. 2008, *ApJ*, 687, 848
- Wang, R., Wagg, J., Carilli, C. L., et al. 2011, *AJ*, 142, 101
- . 2013, *ApJ*, 773, 44
- Willott, C. J., Bergeron, J., & Omont, A. 2015, *ApJ*, 801, 123
- Willott, C. J., Omont, A., & Bergeron, J. 2013, *ApJ*, 770, 13
- Willott, C. J., Albert, L., Arzoumanian, D., et al. 2010, *AJ*, 140, 546
- Wright, E. L., Eisenhardt, P. R. M., Mainzer, A. K., et al. 2010, *AJ*, 140, 1868